Stony Brook University

Scale-up of Reactive Flow through Network Flow Modeling

A Dissertation Presented

by

Daesang Kim

to

The Graduate School

in Partial Fulfillment of the

Requirements

for the Degree of

Doctor of Philosophy

in

Applied Mathematics and Statistics

Stony Brook University

December 2008

Stony Brook University

The Graduate School

Daesang Kim

We, the dissertation committee for the above candidate for the

Doctor of Philosophy degree,

Hereby recommend acceptance of this dissertation.

W. Brent Lindquist,

Dissertation Adviser, Professor, Applied Mathematics and Statistics, Stony Brook University

Xiaolin Li,

Chairperson of Defense, Professor, Applied Mathematics and Statistics, Stony Brook University

Joseph Mitchell,

Professor, Applied Mathematics and Statistics, Stony Brook University

Troy Rasbury

Associate Professor, Geosciences, Stony Brook University

This dissertation is accepted by the Graduate School

Lawrence Martin

Dean of the Graduate School

Abstract of the Dissertation

Scale-up of Reactive Flow through Network Flow Modeling

by

Daesang Kim

Doctor of Philosophy

in

Applied Mathematics and Statistics

Stony Brook University

2008

Pore-throat networks of porous rock samples are constructed from analyses of 3D X-ray computed micro-tomographic (CMT) images of three rock core samples taken from the Viking field in the Alberta basin. The networks are extended to network flow models in order to characterize the properties of reactive flows through porous media. New to both the CMT and network flow work is the extraction of four material phases: the void phase; kaolinite; quartz; and "minerals of interest". Thus, the segmented images contain information on mineral abundances and accessibilities of the four phases: cluster sizes; accessible surface areas; size and area distributions. The standard network flow model is extended to include the mineral distribution network for computation of reactive flow.

Reactions are chosen to simulate precipitation and dissolution reactions that may accompany CO_2 sequestration. The minerals of interest are assumed to be anorthite. The reactive model includes both kinetic and instantaneous reaction components. The reaction rates for kinetic components are integrated over each time step, and the equilibrium condition for the instantaneous components is satisfied at every time step.

The reactive flow model is applied to the Viking samples. The simulation results show that there are differences from previously reported results in the literature. Small reactive surface areas of anorthite result in a slow change in the kaolinite reaction rate; the time to reach a steady state of the kaolinite reaction is on the order of 10^3 seconds. The anorthite reaction rate depends only on pH because of the small values of saturation state. Hence, the pore scale variation of anorthite reaction rate at steady state is small. The simulation results indicate there are heterogeneities in the kaolinite reaction rate, which depends on the saturation state. By inspecting the saturation state, the heterogeneities in the kaolinite reaction rate can be predicted.

Table of Contents

List of Figures

List of Tables

Acknowledgement

First of all, I would like to thank my advisor, Professor Lindquist, for his guidance, support, and encouragement. He provided me of a great chance to start a new study on a new area. I thank committee members, Professor Joseph Mitchell, Professor Xiaolin Li, and Professor Troy Rasbury for their advices and comments on my dissertation. I appreciate Professor Peters' work on BSE and EDX analyses which is basis of part of this work. I thank Joon Dong for teaching a lot of programming skills.

I wish to thank my wife, Moonsun for her love and support of me. I thank my parents and all my family too.

I. Introduction

The anthropogenic use of fossil carbon resources is generating large amounts of atmospheric CO_2, which is the dominant contribution to global warming. There are a number of schemes proposed to reduce the increase in the atmospheric CO_2 load, one of which is storing the CO_2 in the subsurface [1-4]. Such CO_2 sequestration consists of four basic processes; capture, transport, storage, and monitoring. Capture is the process of extracting CO_2 from hydrocarbon combustion. Storage is the process of injecting the captured CO_2 in geologic formations such as deep saline aquifers, depleted oil/gas reservoirs, and unminable coal seams. Deep saline aquifers are numerous and widely distributed and, thus, represent great potential as CO_2 reservoirs. Furthermore, the choice of deep saline aquifers is economically efficient because there are greater chances of finding appropriate groundwater aquifers located near CO_2 sources (such as industrial power plants) thus minimizing transport costs.

To verify that large amounts of CO_2 can safely and efficiently be stored over relevant time scales (centuries to millennia), the subsurface reactive flow in saline aquifers must be completely understood. The reaction kinetics of the CO_2 sequestration process is affected by: host rock type, secondary minerals, faulting and fracturing, as well as pore-level effects. Laboratory measurements on reactive kinetics typically involve crushed, well-mixed samples – thus excluding effects of cementation and pore network access which can result in large difference between reaction rates extracted from laboratory experiments and those observed at the field scale [5]. Reactive flow analyses

need to be performed at the pore scale to catch the micro scale effects, and adequate upscaling techniques are required to obtain parameters for continuum scale simulation [4, 6].

There are a number of studies of pore scale simulation of reactive subsurface flows: [4, 6-10] . In [4], pore scale reactive flow relevant to geological CO_2 sequestration is simulated using network flow modeling, and a methodology is suggested for upscaling from micro scale results to macro scale parameters. A network flow model is one tool to analyze pore scale fluid flow. It can handle single- and multi-phase flow with reactions. The method utilizes a simplified pore-channel network to capture fluid transport through porous rock; it does not include the detailed geometry of each pore or pore-to-pore connection. It can handle a rock sample of the size of a few millimeters to a centimeter.

For the simulation of reactive flow, reactive mineral information is also required. The network used for the simulation in [4] is based upon a network of regular lattice connections with pore and channel properties based upon statistical models. The model considers reactions involving anorthite and kaolinite and involves a system of nine chemical reactions. The simulation in [4] shows that the network flow model captures the heterogeneities in reaction rates. However, the heterogeneities depend highly on the network data and mineral distribution; the simulation results are highly dependent on the conceptual network and mineral distributions used in the simulation.

A growing body of work uses the lattice Boltzmann (LB) method to simulate pore scale reactive flows [6, 8, 10]. The LB method has several advantages. It is simple and flexible, and is appropriate for irregular shaped domains like porous media. Unlike network flow models, the LB method does not need to simplify the pore space. Segmented computed tomographic images can be used directly as the computational

domain with no need for surface construction and difficult grid generation which can be time consuming steps in PDE-based methods. The LB computation results capture the effect of the entire pore geometry resolving concentration gradients and velocities within a pore. Moreover, it does not need tools for analyzing the pore space to extract geometric quantities needed for network flow simulations. The LB method can handle change of pore geometry accompanying dissolution and precipitation, and mineral reactions are treated as boundary conditions on mineral surfaces [10]. The LB method is available for both single-phase and two-phase flow analyses to compute the absolute permeability and relative permeability of a porous rock [11, 12]. However, due to computational complexity, all LB simulation for reactive flow still use conceptual 2-dimensional porous media and conceptual reactions [8, 10].

(a) (b)

Fig. 1. (a) Conceptual network model in [4] and (b) conceptual 2D pore space of a rock in [8] used for pore scale simulation of reactive flow.

The use of synchrotron technology to generate X-ray computed micro-tomographic (CMT) images of rock samples and 3DMA-Rock, a software package for analyses of such CMT images, enable a direct geometrical analysis of pore structure of sedimentary rocks [13-17]. 3DMA-Rock reconstructs the pore-throat network of the

imaged sample by segmentation, medial-axis computation, throat finding, and pore space partitioning. The resulting pore-throat network is a direct basis for network flow models. 3DMA-Rock has been used to identify and analyze images of more than 2 phases: rock, water, and oil [18]. It contains algorithms for multi-phase segmentation, which we adopt (II.2.c) to identify minerals in a CMT image.

Backscatter electron (BSE) and energy dispersive X-ray (EDX) analyses [19] have been used to identify minerals of Viking samples. The BSE analysis was used to produce a four phase segmented image of a sample surface; EDX was used to identify the minerals in each of the four segmented phases. Volume fractions of minerals and surface areas fractions between void phase and minerals were estimated from this analysis. The analyses are indicators for mineral identification, but the analyses cannot directly produce a computational domain for reactive flow simulation since the analyses are 2-dimensional.

The goal of this research is to develop a methodology to construct a network model from real rock, to simulate reactive flow in the network, and to upscale pore scale reaction rates to the continuum scale. Network models were constructed from analysis of three CMT images of Viking samples (a sandstone, a shaly sandstone, and a conglomerate sandstone). A reactive transport flow model is developed using the network model to simulate reactive flow in the Viking samples.

In Section II.1 and 2, we describe the use of CMT to segment the three dimensional Viking samples into four phases in analogy to the BSE analysis of [19]. Mineral distributions for reactive flow modeling are computed based upon the four-phase segmented CMT images. The mineral distributions are included in the reactive pore-throat network.

In Section II.3, we describe the transport model to compute volume flow rate through all channels for reactive flow simulation. In Section II.4, the reactive transport model is presented. The reactive transport model computes the rate of concentration change in a pore by advection, diffusion, and two mineral reactions: anorthite and kaolinite.

In Section 0.1, the three Viking samples are analyzed to construct network models of real rock. In Section 0.0, the network simulation is applied to two of the network models: the sandstone and the conglomerate sandstone. Initially, the porous rock is filled with brine at normal pH. Acidic brine with CO_2 dissolved is then injected into the rock (Fig. 2). The injected brine is transported through the porous rock interacting with accessible minerals. The simulation includes transport of saline water and the aqueous species relevant to mineral reactions. It also includes dissolution and precipitation but ignores any accompanying change of geometry. We analyze the simulation results to examine pore scale effects in the reactive flow and compare the results with those of [4]. Finally, conclusion and future study is discussed in Chapter IV.

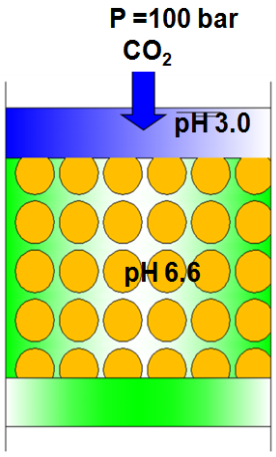

Fig. 2. A schematic diagram of the simulation of the reactive flow. CO_2 dissolved water is injected from the top boundary into porous rock. The flow is similar to the case A in [4].

II. Numerical scheme

1. 3D image analysis

3DMA-Rock is a software package to analyze a 3D X-ray computed micro-tomography (CMT) image of rock sample [13-16]. It uses a grey scale CMT image to identify the pore space and analyze the pore space by four steps: medial axis computation; throat computation; pore-throat network construction. Medial axis is a skeleton of the pore space, and throat computation is based on the obtained medial axis. The pore space is partitioned into pores by throats, and a pore-throat network is constructed by the connectivity of pores and throats. The pore-throat network is a basis of a network flow model for reactive flow simulation. The pore-throat network contains a network structure of the pore space, and throats and medial axis determine the channel properties.

a. Segmentation

Segmentation is the term for image processing algorithm to perform phase identification on a grey-scale image. In this thesis, the kriging based algorithm [17] is used to segment the grey-scale CMT images. The method requires two threshold values, T_0 and T_1. Voxels of intensity less than T_0 are assigned to one phase (Π_0) and voxels of intensity greater than T_1 are assigned to the other phase (Π_1). The identity of the other voxels of intensity between T_0 and T_1 are determined by the kriging algorithm, which uses indicator variables,

$$i(z_c; x_\alpha) = \begin{cases} 1, & \text{if } z(x_\alpha) \le z_c \text{ ,} \\ 0, & \text{otherwise} \quad . \end{cases} \tag{1}$$

Here, $z(x_\alpha)$ is the attenuation coefficient at the position, x_α, and z_c is a chosen threshold value. The probability that $z(x_0) \le z_c$ for voxel, x_0, is estimated by the unbiased linear estimator of the indicator variable,

$$P(z(x_0) \le z_c) = \sum_{\alpha=1}^{n} \lambda_\alpha(z_c; x_0) i(z_c; x_\alpha) \,. \tag{2}$$

The covariance of the indicator variables at two different points is denoted by $C(z_c; x_\alpha - x_\beta) = \mathrm{Cov}(i(z_c; x_\alpha), i(z_c; x_\beta))$. The $\lambda_\alpha(z_c; x_0)$ are obtained by solving the kriging system,

$$\begin{aligned} &\sum_{\beta=1}^{n} \lambda_\beta(z_c; x_0) C(z_c; x_\alpha - x_\beta) + \mu(z_c; x_0) = C(z_c; x_\alpha - x_0) \text{ for } \alpha = 1, \cdots, n \,, \\ &\sum_{\beta=1}^{n} \lambda_\beta(z_c; x_0) = 1 \,, \end{aligned} \tag{3}$$

where $\alpha(= 1, \cdots, n)$ represents neighborhood voxels of x_0. For each unidentified voxel, x_0, the two probabilities, $P_1 = P(z(x_0) \le T_0)$ and $P_2 = P(z(x_0) \ge T_1) = 1 - P(z(x_0) \le T_1)$ are estimated by (2). If $P_1 \ge P_2$, the voxel, x_0 is identified as phase Π_0. Otherwise, the voxel, x_0 is identified as phase Π_1.

In pore-grain segmentation, Π_0 is usually equivalent to the pore phase, and Π_1 to the grain phase. After pore-grain segmentation, clusters of isolated grain voxels which are physically unrealistic are removed (converted to pore phase). Clusters of isolated pore voxels are also removed (converted to grain phase) since such isolated pore space is not accessible to fluid flow.

b. Medial axis

The media axis is a lower dimensional structure containing the basic network topology of the phase in which it is embedded [13]. As it retains a strict geometrical relationship to the phase in which it is embedded. It is useful for the further analyses of the phase structure due to its lower dimensional structure. A medial axis for the pore phase is obtained via a thinning algorithm [20]. Since care is taken to avoid isolated clusters of grain voxels, the medial axis for the pore phase reduces to a network of digitized curves (paths) and vertices (branches). The medial axis computation of a digitized image is sensitive to surface noise. This can result in dead-end branches or the medial axis whose presence contains little to no useful information. All branch-leaf paths of length less than the maximum burn number of the path voxels are deleted by the trimming step [13].

Intuitively, branch clusters corresponds to pores in the network and paths correspond to channels. In fact, a pore body may contain several clusters and the paths which connect them. These occurrences must be identified. We do so by defining “close” clusters. Two clusters are close if the length of a path connecting two clusters is smaller than both distances of the clusters to the closest grain. Two close clusters and the paths

connecting them are conceptually merged into a single cluster unit. After all such merges, the resulting clusters and paths are in 1-1 correspondence with pores and channels respectively [21].

c. Throat computation

A throat is the channel cross section of minimum area corresponding to any position of medial axis path. Throats are important for fluid flow analysis as each represents a bottleneck to the flow along its channel. In 3DMA-Rock, throats are used to partition the void space into pore bodies (separated by throats). 3DMA-Rock utilizes three algorithms for throat computation, a "wedge based" algorithm, Dijkstra shortest path algorithm [13, 16], and the maximal balls algorithm [22]. We utilize the first two in this work.

The wedge based algorithm constructs a local grain boundary for each medial axis path by a grass fire algorithm and constructs a rough approximation to the cross section perimeter on the local grain boundary for each voxel on the medial axis. The algorithm then compares the cross section areas determined by the rough perimeters locating the minimum cross section area. A finer reconstruction of the minimum area perimeter is computed and a triangulation performed to construct the spanning surface. This triangulated surface is defined to be the throat.

The Dijkstra based algorithm dilates the medial axis path radially and sequentially records the surface grain voxels that are encountered by the dilated object. The growing set of encountered grain voxels is searched (via Dijkstra algorithm) to find a loop enclosing the medial axis. The first occurrence such a constructable loop is determined to

be the throat perimeter for the path.

First, the wedge based algorithm is applied to all medial axis paths. To the medial axis path on which the wedge based algorithm failed to find a throat, the Dijkstra based algorithm is applied to find a throat. After this, two sets of throats computed are merged into a full set of throats [21].

d. Pore-throat network construction

To construct a pore-throat network, the void space is partitioned into pore bodies. Each pore body is delimited by surface of grain voxels and by throat barriers. We compute pore volume, pore surface area, coordination number, and principal diameters for each pore [21, 23]. The principal diameters are pore widths in the three principal directions in which the products of inertia vanish. With the obtained pores, we can construct pore-throat network by using the pore-pore connectivity and pore-throat connectivity.

2. Pore-throat network of mineral distributions

The rates of production and consumption of a species by a chemical reaction are proportional to the reaction rate and the reactive surface area. The distributions of minerals and reactive surface areas are crucial for a reactive flow analysis. A previous research used conceptual network and mineral distributions for network flow simulation [4], and another research used conceptual pore space and mineral distribution [8] for reactive flow simulations as shown in Fig. 1. In this section, a new methodology is introduced to compute the distributions of minerals and reactive surface areas of Viking samples for the simulation of reactive flow through the rock samples.

The results of backscatter electron (BSE) and energy dispersive X-ary (EDX) analyses [19] done by Peters are referred to identify minerals in the Viking samples. BSE analysis produces a four phase segmented image of a sample surface, and EDX captures minerals at some points to identify minerals in each phase of BSE images. 3D CMT images of the Viking samples are segmented into four phases corresponding to BSE images. The mineral distributions of the Viking samples are computed using the four-phase CMT images. Furthermore, a pore-throat network is constructed for a four-phase CMT image, and the mineral distributions are added to the pore-throat network to construct a network model. The network model is used for simulation of reactive flow in Section II.4.

a. Viking sample

Three Viking samples, Viking3W4, Viking10W4, and Viking 14w5 which are described as sandstone, shaly sandstone, and conglomerate sandstone respectively are

analyzed to construct the pore-throat networks of mineral distributions. The three Viking samples are real rock samples from the abandoned oil/gas reservoirs in the Viking formation in the Alberta basin. The samples are imaged at the X2B beam line at the National Synchrotron Light Source at Brookhaven National Laboratory. The resolution of the CMT images is 3.98μm and the size is originally 723×723×600. The images are resized to remove regions of bad image quality, and the sizes of resized Viking3W4, Viking10W4, and Viking14W5 are 723×723×356, 723×723×405, and 723×723×405 respectively. The corresponding real dimensions of the resized CMT images are 2.88×2.88×1.42 mm^3, 2.88×2.88×1.61 mm^3, and 2.88×2.88×1.61 mm^3 respectively.

b. BSE and EDX analyses

A scanning electron microscope (SEM) is used in backscatter mode to generate images by counting backscattered electrons (BSE). The number of backscattered electrons is proportional to the mean atomic number (MAN) on the scanned surface element. The MAN surface map thus generated produces an image of mineralogical variation on the surface. However, unique identification of minerals is not, in general, possible as different minerals can bare similar MANs. Energy dispersive X-ray (EDX) analysis generates a spectrum of emitted X-ray energies for each point on a sample surface. EDX is therefore used to identify minerals on the surface by the chemical composition. EDX is much more time consuming than BSE. EDX can be used on small patches to identify species present, and BSE can be used over larger areas to infer the distribution of these species.

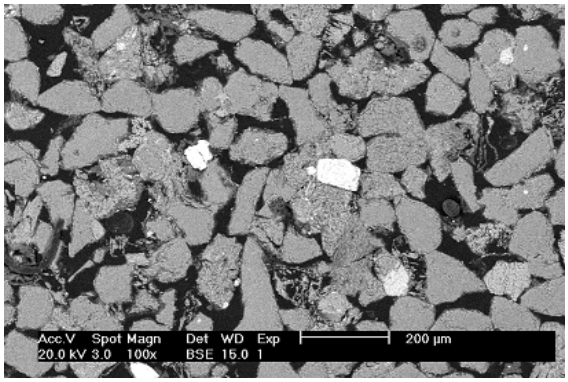

(a)

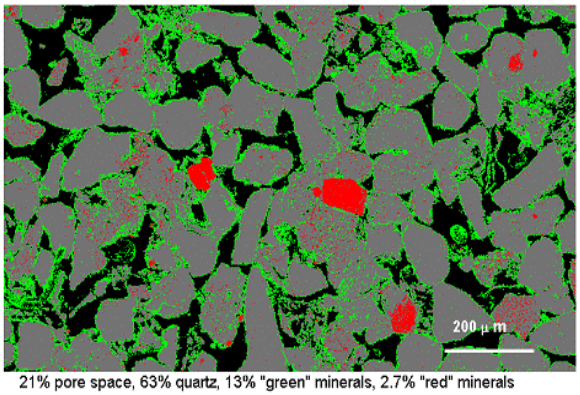

(b)

Fig. 3. (a) The grey scale BSE image of Viking3W4. (b) The segmented image of the grey scale BSE image. Black, green, grey, and red indicate void phase, minerals of MAN < MAN_{quartz}, quartz, and minerals of MAN > MAN_{quartz}.

The images in the Fig. 3 are sample BSE images of Viking 3W4 provided by Peters [19]. The dominant mineral of the rock is quartz. Minerals are separated into three categories: quartz, MAN < MAN_{quartz}, and MAN > MAN_{qaurtz}. This segmented image of the Viking3W4 sample is shown in the Fig. 3(b). Using EDX analysis, the minerals in each color range can be identified. Minerals with MAN less than quartz include kaolinite, albite, and Mg chlorite. Minerals with MAN greater than quartz include anorthite, K-feldspar, and apatite.[19]. For a convenience in this thesis, the four names, void, kaolinite,

quartz, and minerals of interest (MoI) are used for the four phases, black, green, grey, and red respectively.

c. Mineral distributions of pore-throat network

In a new application of CMT, following the idea of the four-phase BSE analysis described in the previous section the CMT images were segmented into four phases. The four phases are void, quartz, attenuation coefficient (AC) less than quartz, and AC greater than quartz. The hope of course is that the AC segmentation captures that of MAN.

At X-ray energies of 25-30 keV at which the CMT images were produced, the attenuation coefficient (AC) is dominated by the photoelectric effect (PE). The cross section for σ_{PE} for the photoelectric effect is proportional to $Z^{4.5}$ where Z is the atomic number of the scattering atom. The AC for a mineral is a linear combination of the cross section's σ_{PE} of its constituents, e.g., $\sigma_{SiO_2} = \sigma_{Si} + 2\sigma_O \sim Z_{Si}^{4.5} + 2Z_O^{4.5} \approx \left(\frac{Z_{Si}+2Z_O}{3}\right)^{4.5}$. Thus, CMT is sensitive to atomic number, but is not proportional to the MAN as is BSE. Thus, though some identification difference is expected in the presence of reasonably few minerals. CMT and BSE analyses should produce results that are comparable. CMT has the advantage that 3D mineral distributions can be obtained.

Three iterations of bi-phase segmentation are used to assign one of four phases to each voxel. The first iteration is used to identify the primary pore space (void space + kaolinite) and the primary grain space (quartz + MoI). The second iteration is applied to the primary pore space to segment the void space and kaolinite. This method avoids losing void phase, the least X-ray attenuated phase by blocking the effect of higher attenuated phases-kaolinite and MoI- around the void phase. The third iteration is applied

to the primary grain space to identify kaolinite and MoI in the segmented primary grain space.

The resolution, 3.98 μm of the CMT images is coarser than the resolution, 1.8 μm of the BSE images for the mineralogical analysis. Edge and finite volume effects therefore mean that the CMT analysis will tent to result in smaller measures of void space and MoI phases, and especially, smaller surface areas between these two phases than those derived from the BSE analysis. This error is particularly prevalent when the void phase and MoI are adjacent to each other. A correction is needed to obtain CMT results that are more consistent with the BSE results. The correction step consists of an application of morphological dilation. MoI phase is dilated outward by a distance of one to two voxels. After dilation, each dilated voxel is examined. If a dilated voxel neighbors a void voxel, it is permanently reassigned as MoI phase. If it does not neighbor any void voxel, the dilated voxel remains as its originally assigned phase. This process can remove some voxels of incorrectly assigned kaolinite and quartz phases, and it can recover void and MoI voxels and the inter-phase surface area between void phase and MoI. A similar procedure is applied to the void phase to increase the void space near MoI.

Any remaining unrealistic/inappropriate voxels are then removed from the segmented images. Any cluster of mineral voxels surrounded by the void space is physically unrealistic, and the “floating” cluster is “removed” by converting it to void phase. All isolated primary pore voxels (void space + kaolinite) surrounded by the primary grain space (quartz + MoI) are converted to the quartz phase. The rationale for this is that fluid cannot reach such isolated primary pore regions.

For further analyses, two types of segmented images, the four-phase segmented images and bi-phase primary pore/primary grain segmented images are used for

mineralogical analysis and pore-throats network construction, respectively. The images processed above produce the final segmented images for the mineralogical analysis. The bi-phase images (primary pore phase and primary grain) are processed further by "deleting" all clusters of primary grain voxels "floating" in the primary pore space. This results in the final images for mineral information and those for pore-throat network being slightly different. However, the difference is very small, e.g., it is less than 0.1% in the case of Viking3W4. The bi-phase image is used to construct a pore-throat network of the primary pore space, and the four-phase image which contains all mineral information is used to add the mineral distributions to the pore-throat network.

After segmentation, a pore-throat network of the primary pore space is constructed. This network will allow correlation of the mineral distribution in the sample with the pore structure. As described in the previous section, there are several needed to construct the pore-throat network: medial axis computation; throat finding; and partitioning of the pore space.

For each pore body of the primary pore space, the mineral distributions of the pore body are determined by computing the volumes of mineral phases inside of and touching the pore body and the surface areas between two different phases inside the pore.

The Fig. 4 is a cartoon of a pore connected to three other pores via three channels. The pore is partly occupied by kaolinite phase. Two MoI "grains" touch the pore. The rest of the pore is surrounded by quartz. The cartoon illustrates the quantities of interest for reactive flow modeling: the pore volume; kaolinite volume, V_G, in the pore, and volumes, V_{R1}, V_{R2}, of the connected MoI. The surface areas accessible from the pore body are computed: the area, S_{RB}, of MoI exposed to void and the area, S_{GB}, of the kaolinite exposed to void. S_{RB} and S_{GB} denote mineral surface areas accessible directly from the

pore. The area, S_{RG}, of MoI coated by the kaolinite is also computed. Other surface areas, such as the area, S_{BQ}, between void phase and quartz and the area, S_{GQ}, between kaolinite and quartz are also computed. The pore volume, V_{pore}, and pore surface area, S_{pore}, in Fig. 4 are (V_G+V_B) and $(S_{RG}+S_{GQ}+S_{RB}+S_{BQ})$.

The volumes for pore body, void phase, kaolinite, and MoI are computed by voxel counting, and the surface areas are computed by the marching cubes algorithm [23, 24]. The marching cubes algorithm is used for surface construction in a bi-phase image. The algorithm uses a dual grid; it constructs and triangulates surfaces by inspecting all eight edges of each cube of the dual grid. There are 256(=2^8) total possible configurations, of which only 15 are unique configurations. The other configurations are generated by

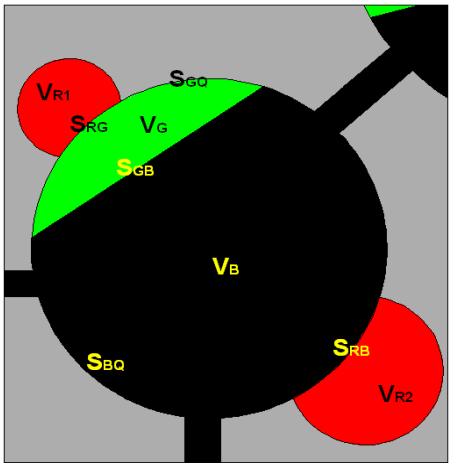

Fig. 4. One pore body contains kaolinite (green) inside and it neighbors two clusters of MoI (red). Black and grey colors represent void space and quartz space respectively. S denotes surface areas between two minerals or mineral and void space. V denotes volumes of mineral clusters.

rotation and reflection of these15. Surface area is computed based on constructed surface triangles. For the four-phase images, two applications of the marching cubes algorithm

are needed to construct the inter-phase surface between all pairs of phases. Let P_1 and P_2 be two phases for which the inter-phase surface is to be computed. Let $B_1 = P_1$ and $B_2 = I \backslash P_1$ (complement to P_1 in the image I). The marching cubes algorithm is applied to the construction of the B_1, B_2 inter-phase surface. Let S_1 denote the surface. Next, let $B_2 = P_2$ and $B_1 = I \backslash P_2$. Apply the marching cubes algorithm to construct the B_1, B_2 surface and label it S_2. Let $S_1 \cap S_2$ denote the vertices and triangles common to both surfaces. Then, $S_1 \cap S_2$ is the desired P_1, P_2 surface except for some "missing" surface edge.

The surface areas computed from CMT images are small and not appropriate for reactive surface areas because CMT images have a finite resolution coarser than a molecular size. The computed surface areas are corrected by the BET surface area. The BET (Brunauer, Emmett and Teller) method is based on the multilayer adsorption of gas molecules on a solid surface [25]. It estimates the number of molecules adsorbed in the first layer on the solid surface and computes the surface area by multiplication of the number of molecules and the surface area that one molecule occupies. The BET surface area of the Viking 3W4 sample was measures giving a specific surface area measurement of 40,000 cm^{-1}. Thus, surface areas as measured via CMT analysis were corrected by a multiplicative constant to ensure that the total pore grain specific surface area in the imaged region, as measured by CMT, agrees with the BET measured value. The surface areas of the other rock samples are also corrected by multiplying the factor.

3. Single-phase network flow model

a. Construction of the single-phase network flow model

The reactive flow problem in this research is a multi-species flow through porous rock with chemical reactions. Thus, a transport model is needed, and a network flow model is used to compute flow rates in porous rock. Based on the pore-throat network computed by the previous procedure, we can easily construct the single-phase network flow model[26, 27]. Network flow models typically simplify the pore space to a network of pores and channels. The pore bodies comprise all the pore volume while channels control flows. Thus, a pore in the network described in Section 1.d becomes a pore in the network flow model while a throat in the network corresponds to a channel in the network flow model.

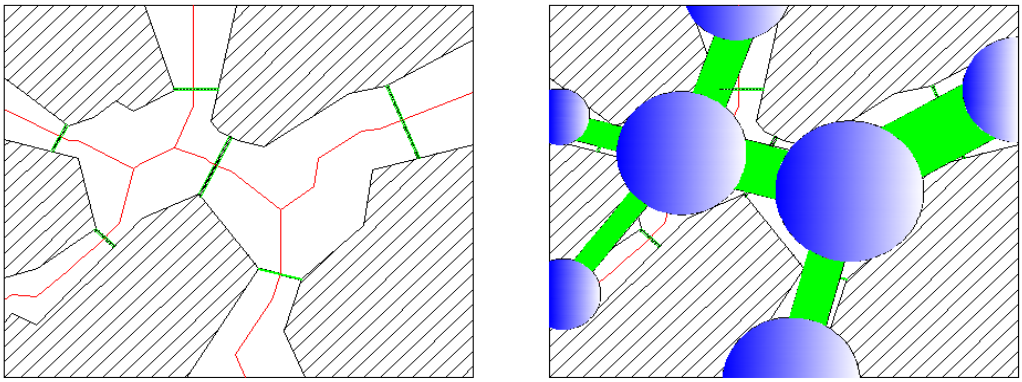

(a) (b)

Fig. 5. (a) A 2D example of a constructed pore-throat network. (b) Schematic of network flow model developed from the pore-throat network in (a).

The flow through the whole network is driven by the pressure difference between inlet and outlet. We assume that a pressure is constant in a pore and the flow rate through

a channel is caused by the pressure difference between the connected pores. The goal of the single-phase network flow model is to compute the absolute permeability of the rock, pressure of pores, and flow rates through all channels. The absolute permeability of a rock is defined by [28],

$$K = \frac{\mu Q L}{A \Delta P} \tag{4}$$

μ[kg/m·s] is the viscosity of the fluid, Q [m^3/s] is the volume flow rate through the porous rock, A is the cross-section area of the sample normal to flow direction, L is the length of the rock in the flow direction, and ΔP [kg/m·s^2] is the pressure difference between the inlet and outlet boundaries. The channel conductance, C_{ij} from pore *i* to pore *j* is defined by

$$Q_{ij} = C_{ij}(P_i - P_j) \tag{5}$$

where Q_{ij} is the volume flow rate from pore *i* to pore *j*, and P_i and P_j are pressures of pore *i* and pore *j* respectively. Note C_{ij}=C_{ji}, i.e., conductance is not directional. For each pore *i*, the net flow rate should be zero to satisfy mass conservation,

$$\sum_j Q_{ij} = C_{ij}\left(P_i - P_j\right) = 0, \tag{6}$$

where the sum is over the neighboring pores. Let P_{in} and P_{out} be pressures at the inlet and outlet. Pores are divided into three classes – those that directly connect to the inlet, those

directly connect outlet, and the reminder, which refer to as “interior” pores. The pressures of these interior pores are unknown. Application of (6) to all interior pores produces a system of N_p linear equations with N_P unknown pore pressures. The coefficient matrix is real, symmetric, sparse, diagonally dominant matrix. We utilize a sparse, preconditioned conjugate-gradient solver for the linear system to obtain pore pressure [29, 30]. With the computed pore pressures, the volume flow rate through each channel follows from (5). The bulk volume flow rate and absolute permeability are computed by (4).

b. C_{ij} based on channel shape factor

If we assume the cross section of a channel is constant, then we can obtain the channel conductance by solving the 2-dimensional elliptic Poisson equation for Poiseuille’s flow through the channel [31],

$$\mu\nabla^2\vec{u} - \nabla P = 0,\ \vec{u} = 0 \text{ on the wall,} \tag{7}$$

where $\vec{u}$ is flow velocity, and ∇P is the pressure gradient in the flow direction. ∇P is constant because the channel flow is assumed to be fully developed. The Poisson equation can be solved numerically for the conductance of triangular cross sections. Based on the many numerical solutions, [26] has noted that

$$\tilde{g} = g\frac{\mu}{A^2} \approx \frac{3}{5}G, \tag{8}$$

where $\tilde{g}$ is the dimensionless hydraulic conductance, A is the cross section area, G is the shape factor, $G=A/P^2$, and P is the perimeter of the cross section [32]. Similarly, we can derive a cross sectional shape factor for a pore, $G_p = \frac{VD}{S^2}$ [27] where V is the pore volume, D is a pore diameter, and S is the pore surface area. With the assumption of triangular cross section for pores, we can use the equation, $\tilde{g}_p \approx \frac{3}{5} G_p$ for the dimensionless hydraulic conductance of a pore. The maximum shape factor for triangles is that of an equilateral triangle, $G_{T,max} = \sqrt{3}/36$. For a throat having shape factor greater than $G_{T,max}$, the assumption of triangular cross section is not appropriate. In such cases, the channel cross section is assumed to be either rectangular or elliptic. Analytic computations by [26, 27, 31, 33] have determined the relationship between dimensionless conductance and shape factor for rectangular and ellipses. Incorporating these results gives

$$\tilde{g} = \begin{cases} 0.6G, & 0 \le G \le G_{T,max}, \\ 0.56G, & G_{T,max} \le G \le G_{R,max}, \\ 0.5G, & G_{R,max} \le G \le G_{E,max}, \end{cases} \tag{9}$$

which can be used for both pores and channel conductance. Here, $G_{T,max} = \sqrt{3}/36, G_{R,max} = \frac{1}{16}$, and $G_{E,max} = 1/4\pi$ are the maximum shape factors of triangles, rectangles, and ellipses respectively. The above equation is used for the dimensionless hydraulic conductances of both throat and pore. Since the conductance between two pores cannot be realistically expressed by a single constant cross section, the conductance, C_{ij}, is expressed via a series resistance model incorporating the throat and one half of each of connected pores,

$$C_{ij} = \left(\frac{d_t}{g_t} + \frac{1}{2}\left(\frac{d_i}{g_i} + \frac{d_j}{g_j} \right) \right)^{-1}, \tag{10}$$

where d_t, d_i, and d_j are the lengths of the throat, pore i, and pore j respectively. The total length $d_t+d_i+d_j$ is set to be the length, d_0 of the corresponding medial axis path. We use a weight, ω to assign the throat length d_t, and we set the pore lengths proportional to the pore principal diameters. Then, the three lengths are

$$d_t = \omega d_0, \qquad d_i = \frac{(1-\omega)D_i}{D_i + D_j} d_0, \qquad d_j = \frac{(1-\omega)D_j}{D_i + D_j} d_0$$

A proper choice of ω is required for the network and experimental data [34] can be used to estimate the best value of ω.

4. Reactive transport model

Saline water with dissolved CO_2 is injected into the sample core and the saline water is transported through the porous rock interacting with accessible minerals (Fig. 2). The saline water is highly acidic because CO_2 is dissolved under high pressure. The simulation includes transport of saline water and some aqueous species relevant to mineral reactions. We use the network model and mineral distribution explained in Section II.2.c for the reactive flow simulation. The network flow model in Section II.3 is

used to compute volume flow rates through all channels for the simulation. In this reactive flow simulation, all fluid properties such as concentration and reaction rates are constant in a pore. The reactions occurring among the chemical species which are captured by the following ordinary differential equation which captures species advection, diffusion, and kinetic reactions with minerals [4]. For each pore *i*,

$$V_i \frac{d[\cdot]_i}{dt} + \sum_{Q_{ij}>0} Q_{ij}[\cdot]_i + \sum_{Q_{ij}<0} Q_{ij}[\cdot]_j = S_{i,[\cdot]} + \sum_j D_{[\cdot]} a_{ij} \frac{[\cdot]_j - [\cdot]_i}{l_{ij}}, \quad (11)$$

where $_j$: index of a neighboring pore,

V_i : pore volume of pore *i*,

$[\cdot]_i$: concentrations of species,

Q_{ij} : volume flow rate from pore *i* to pore *j*,

$D_{[\cdot]}$: diffusion coefficients of species · ,

a_{ij} : throat area between pore *i* and pore *j*,

$S_{i,[\cdot]}$: kinetic reaction source term of the species · in pore *I*,

$S_{i,[\cdot]} = (r_A A_A + r_K A_K)_{[\cdot]}$,

r_A, r_K : anorthite and kaolinite reaction rates of pore *i*,

A_A, A_K: surface areas of anorthite and kaolinite in pore *i*.

For the anorthite and kaolinite reactions in (11), the kinetic reaction model is explained in the next section. The reaction model for reactive flow has 9 instantaneous

reactions. The 9 instantaneous reactions are assumed to be in equilibrium since the reaction rates are fast. Equilibrium computation is introduced in Section II.4.b. We solve the coupled pore system (11) numerically by the Euler method [35].

a. Kinetic reactions

In (11), the term $S_{i,[\cdot]} = (r_A A_A + r_K A_K)_{[\cdot]}$ is the sum of anorthite and kaolinite reactions [4, 36]. The anorthite reaction is

$$CaAl_2Si_2O_8(s)+8H^+ \leftrightarrow Ca^{2+}+2Al^{3+}+2H_4SiO_4$$

and the kaolinite reaction is

$$Al_2Si_2O_5(OH)_4(s)+6H^+ \leftrightarrow 2Al^{3+}+2H_4SiO_4+H_2O.$$

The reaction rates, r_A, r_K are modeled as [4, 36]

$$r_A = \left(k_H\{H^+\}^{1.5} + k_{H_2O} + k_{OH}\{OH\}^{0.33}\right)(1-\Omega_A), \tag{12}$$

with

$$\Omega_A = \frac{\{Ca^{2+}\}\{Al^{3+}\}^2\{H_4SiO_4\}^2}{\{H^+\}^8 K_{eq,A}}, \tag{13}$$

and the reaction rate of kaolinite is

$$r_K = (k_H\{H^+\}^{0.4} + k_{OH}\{OH\}^{0.3})\left(1-\Omega_K^{0.9}\right), \tag{14}$$

with

$$\Omega_K = \frac{\{Al^{3+}\}^2\{H_4SiO_4\}^2}{\{H^+\}^6 K_{eq,K}}. \quad (15)$$

In (12-15), Ω is the saturation state indicating over- or under-saturation. Under-saturation, $\Omega < 1$, results in dissolution of the corresponding mineral; over-saturation, $\Omega > 1$, results in solute precipitation. $\{\cdot\}$ is the activity of a species discussed in Section 4.e.

The reaction rate constants at 25°C and the equilibrium constant at 50°C of anorthite and kaolinite are listed in Table 1. A simulation temperature of 50°C is typical for CO_2 sequestration depths, so the reaction rates are adjusted by the Arrhenius equation [37],

$$\frac{k}{k_0} = e^{-E_{Ar}\left(\frac{1}{RT}-\frac{1}{RT_0}\right)}, \quad (16)$$

where E_{Ar} is the activation energy. The adjusted reaction rates at 50°C are also listed in Table 1.

The reaction rates, (12) and (14) can be expressed by

$$r = f_{pH} \times f_{\Omega}. \quad (17)$$

Here,

$$f_{pH} = k_H\{H^+\} + k_{H_2O} + k_{OH}\{OH^-\}, \quad (18)$$

$$f_{\Omega} = (1 - \Omega^m). \quad (19)$$

f_{pH} and f_{Ω} determine the reaction rates. f_{pH} is a function of pH, and the value of f_{pH} is shown in Fig. 6. f_{pH} has its minimum when pH is around 6.

Table 1. Equilibrium K_{eq} and reaction rate k constants for anorthite and kaolinite

	log K_{eq} (50°C)		log k (mol/m^{2}s)			E_{Ar}(kJ/mol)
			log k_H	log k_{H2O}	log k_{OH}	
Anorthite	21.7	25°C	-3.32	-11.6	-13.5	-18.4
		50°C	-3.07	-11.35	-13.25	
Kaolinite	3.80	25°C	-10.8	-	-15.7	-29.3
		50°C	-10.40	-	-15.30	

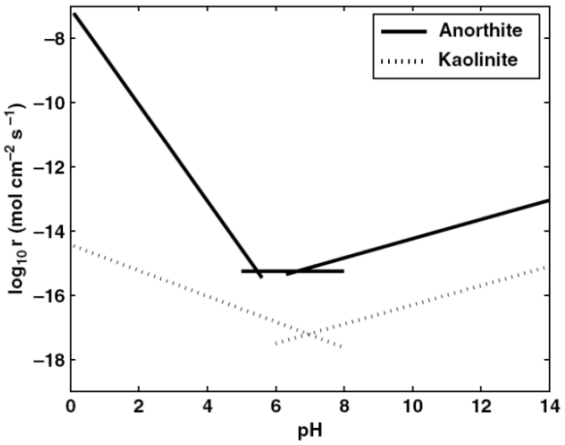

Fig. 6. f_{pH} of anorthite and kaolinite as a function of pH [4].

b. Equilibrium computation of instantaneous reactions

The simulation considers water and 14 aqueous species, H_2O, H^+, OH^-, H_2CO_3, HCO_3^-, CO_3^{2-}, H_4SiO_4, $H_3SiO_4^-$, $H_2SiO_4^{2-}$, Al^{3+}, $Al(OH)^{2+}$, $Al(OH)_2^+$, $Al(OH)_3$, $Al(OH)_4^-$, and Ca^{2+}. There are 9 important chemical reactions for the simulation. Table 2 shows the 9 instantaneous reactions with equilibrium constants [4, 38]. The reaction rates of the 9 reactions are so fast that the 9 reactions are assumed to be in equilibrium at any time [4]. We need to compute the equilibrium state of the 9 instantaneous reactions. The simulation first, computes the reactive transport model to apply the advection, diffusion, and the two kinetic reactions of anorthite and kaolinite during the time step, Δt. The equilibrium computation of the instantaneous reactions follows. The Fig. 7 depicts the above simulation procedure.

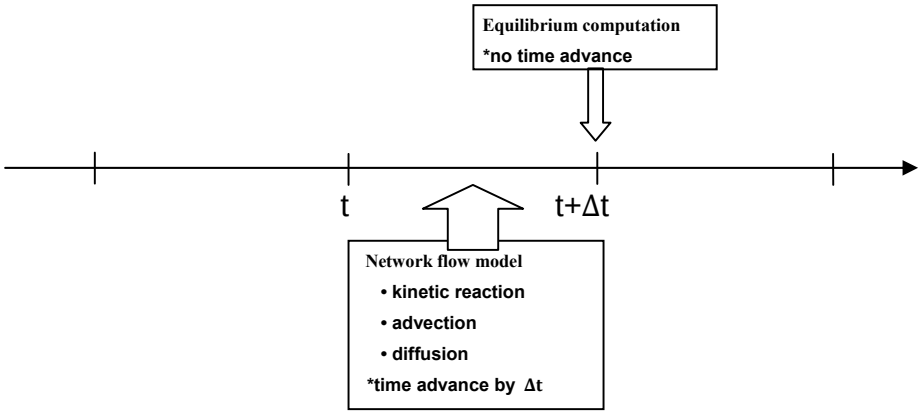

Fig. 7. One time step in the simulation

The first step of the equilibrium computation is the selection of components from the 15 species. A smallest set of species characterizing the chemical system is defined as components [37]. There are 15 species and 9 reactions, and thus, 6 species should be used

for the set of components. There are several appropriate choices of components; one choice is { H_2O, H^+, H_2CO_3, H_4SiO_4, Al^{3+}, and Ca^{2+} }. Then, the activities of the other secondary species can be expressed by the activities of the 6 selected components. Table 3 shows the 9 derived equilibrium equations of the instantaneous reactions to compute the activities of the secondary species. The left hand side of each reaction is a secondary species, and the right hand side is composed of a few species of the components. The Ca^{2+} appears in the simulation by the kinetic reactions but there is no instantaneous reaction of Ca^{2+}. [Ca^{2+}] is not changed by the equilibrium computation.

Table 2. Instantaneous reactions and equilibrium constants.

	Reactions	$\log K_{eq}$
1.	$H_2O \Leftrightarrow H^+ + OH^-$	-13.2
2.	$H_2CO_3^* \Leftrightarrow HCO_3^- + H^+$	-6.15
3.	$HCO_3^- \Leftrightarrow CO_3^{2-} + H^+$	-10.0
4.	$H_4SiO_4 \Leftrightarrow H_3SiO_4^- + H^+$	-9.2
5.	$H_3SiO_4^- \Leftrightarrow H_2SiO_4^{2-} + H^+$	-12.4
6.	$Al^{3+} + OH^- \Leftrightarrow Al(OH)^{++}$	8.76
7.	$Al^{3+} + 2OH^- \Leftrightarrow Al(OH)_2^+$	18.9
8.	$Al^{3+} + 3OH^- \Leftrightarrow Al(OH)_3$	27.3
9.	$Al^{3+} + 4OH^- \Leftrightarrow Al(OH)_4^-$	33.2

Table 3. 9 Derived instantaneous reactions, and corresponding equilibrium equations to compute the activities of the secondary species.

	Reactions	$\log K_{eq}$	
1.	$H_2O - H^+ \Leftrightarrow OH^-$	-13.2	$\{OH^-\} = K_1\{H_2O\}\{H^+\}^{-1}$
2.	$H_2CO_3^* - H^+ \Leftrightarrow HCO_3^-$	-6.15	$\{HCO_3^-\} = K_2\{H_2CO_3^*\}\{H^+\}^{-1}$
3.	$H_2CO_3^* - 2H^+ \Leftrightarrow CO_3^{2-}$	-16.15	$\{CO_3^{2-}\} = K_3\{H_2CO_3^*\}\{H^+\}^{-2}$
4.	$H_4SiO_4 - H^+ \Leftrightarrow H_3SiO_4^-$	-9.2	$\{H_3SiO_4^-\} = K_4\{H_4SiO_4\}\{H^+\}^{-1}$
5.	$H_4SiO_4 - 2H^+ \Leftrightarrow H_2SiO_4^{2-}$	-21.6	$\{H_2SiO_4^{2-}\} = K_5\{H_4SiO_4\}\{H^+\}^{-2}$
6.	$Al^{3+} + H_2O - H^+ \Leftrightarrow Al(OH)^{++}$	-4.44	$\{Al(OH)^{++}\} = K_6\{Al^{3+}\}\{H_2O\}\{H^+\}^{-1}$
7.	$Al^{3+} + 2H_2O - 2H^+ \Leftrightarrow Al(OH)_2^+$	-7.5	$\{Al(OH)_2^+\} = K_7\{Al^{3+}\}\{H_2O\}^2\{H^+\}^{-2}$
8.	$Al^{3+} + 3H_2O - 3H^+ \Leftrightarrow Al(OH)_3$	-12.3	$\{Al(OH)_3\} = K_8\{Al^{3+}\}\{H_2O\}^3\{H^+\}^{-3}$
9.	$Al^{3+} + 4H_2O - 4H^+ \Leftrightarrow Al(OH)_4^-$	-19.6	$\{Al(OH)_4^-\} = K_9\{Al^{3+}\}\{H_2O\}^4\{H^+\}^{-4}$

From Table 3, we know all activities when the component activities are given. The activity coefficients are used to compute the activities [37] by,

$$\{\cdot\} = \gamma[\cdot]. \tag{20}$$

We will discuss the computation of the activity coefficients and activities in Section II.4.e.

The equilibrium state satisfies the mass balance of the species. Masses of species are not conserved, but masses at equilibrium are balanced by the chemical reactions. We use new variables, the total concentrations to apply the mass balance [37]. For example, the total concentration of $H_2CO_3^*$ is defined by $TOT[H_2CO_3^*] = [H_2CO_3^*]+[HCO_3^-]+[CO_3^{2-}]$. Let the subscript, $_0$ denote given concentrations of the species out of

equilibrium and the subscript, $_{eq}$ denote the concentrations of the given species in equilibrium. Then, $TOT[H_2CO_3^*]_0 = [H_2CO_3^*]_0 + [HCO_3^-]_0 + [CO_3^{2-}]_0$ and $TOT[H_2CO_3^*]_{eq} = [H_2CO_3^*]_{eq} + [HCO_3^-]_{eq} + [CO_3^{2-}]_{eq}$. While $[HCO_3^-]$ increases from $[HCO_3^-]_0$ to $[HCO_3^-]_{eq}$ by the chemical reaction #2 in Table **3**, the same amount of $[H_2CO_3^*]$ is consumed by the reaction. If $[HCO_3^-]$ decreases, then the same amount of $[H_2CO_3^*]$ is produced. Likewise, the change of $[CO_3^{2-}]$ induces the change of $[H_2CO_3^*]$ in the opposite direction by the instantaneous reaction #3 in Table 3. Thus, $TOT[H_2CO_3^*]$ is conserved, i.e., $TOT[H_2CO_3^*]_0 = TOT[H_2CO_3^*]_{eq}$. The total concentrations of all components are conserved in equilibrium, i.e., $TOT[\cdot]_0 = TOT[\cdot]_{eq}$ for all components [37]. The total concentrations of all components are listed in Table 4.

Table 4. Total concentrations of all components.

Components	$TOT[\cdot]$
H_2O	$[H_2O]+[OH^-]+[Al(OH)^{++}]+2[Al(OH)_2^+]+3[Al(OH)_3]+4[Al(OH)_4^-] \simeq [H_2O]$
H^+	$[H^+]-[OH^-]-[HCO_3^-]-[CO_3^{2-}]-[H_3SiO_4^-]-[H_2SiO_4^{2-}]$ $-[Al(OH)^{++}]-[Al(OH)_2^+]-[Al(OH)_3]-[Al(OH)_4^-]$
$H_2CO_3^*$	$[H_2CO_3^*]+[HCO_3^-]+[CO_3^{2-}]$
H_4SiO_4	$[H_4SiO_4]+[H_3SiO_4^-]+[H_2SiO_4^{2-}]$
Al^{3+}	$[Al^{3+}]+[Al(OH)^{++}]+[Al(OH)_2^+]+[Al(OH)_3]+[Al(OH)_4^-]$
Ca^{2+}	$[Ca^{2+}]$

Table 5 contains the whole information for the equilibrium computation of the 9 instantaneous reactions. The first 6 rows of Table 5 are for the 6 components; the

remaining 9 rows are for 9 secondary species. The rows of the secondary species contain the exponents and the equilibrium constants of the derived 9 equilibrium equations in Table 3. The columns of components of Table 5 show the species and coefficients for the total concentrations of components.

Using Table 5, we can compute the activities of all species if the activities of the 6 components are given. The concentrations of all species are obtained by dividing the activities by the corresponding activity coefficients. Thus, the problem of equilibrium computation is how to find the activities of 6 components which satisfy mass balance, i.e. conservation of total concentrations of 6 components. When we estimate a set of activities of the components, we can compute the difference, $\Delta TOT[\cdot]_{\mathrm{gs}} = TOT[\cdot]_{\mathrm{gs}} - TOT[\cdot]_0$ between the total concentrations from the estimated component activities and the total concentrations of the given concentrations, $[\cdot]_0$. Let F() be the $\mathbb{R}^6 \rightarrow \mathbb{R}^6$ function,

$$\begin{aligned} &\mathrm{F}\left(\{\mathrm{H_2O}\}_{\mathrm{gs}}, \{\mathrm{H^+}\}_{\mathrm{gs}}, \{\mathrm{H_2CO_3^*}\}_{\mathrm{gs}}, \{\mathrm{H_4SiO_4}\}_{\mathrm{gs}}, \{\mathrm{Al^{3+}}\}_{\mathrm{gs}}, \{\mathrm{Ca^{2+}}\}_{\mathrm{gs}} \right) \\ &= \left(\Delta TOT[\mathrm{H_2O}]_{\mathrm{gs}}, \Delta TOT[\mathrm{H^+}]_{\mathrm{gs}}, \Delta TOT[\mathrm{H_2CO_3^*}]_{\mathrm{gs}}, \Delta TOT[\mathrm{H_4SiO_4}]_{\mathrm{gs}}, \right. \\ &\quad \left. \Delta TOT[\mathrm{Al^{3+}}]_{\mathrm{gs}}, \Delta TOT[\mathrm{Ca^{2+}}]_{\mathrm{gs}} \right) . \end{aligned} \tag{21}$$

At the equilibrium component activities,

$$\mathrm{F}\left(\{\mathrm{H_2O}\}_{\mathrm{eq}}, \{\mathrm{H^+}\}_{\mathrm{eq}}, \{\mathrm{H_2CO_3^*}\}_{\mathrm{eq}}, \{\mathrm{H_4SiO_4}\}_{\mathrm{eq}}, \{\mathrm{Al^{3+}}\}_{\mathrm{eq}}, \{\mathrm{Ca^{2+}}\}_{\mathrm{eq}} \right) = (0, 0, 0, 0, 0, 0)$$

because the total concentrations, *TOT*[·] is conserved in the equilibrium computation; $\Delta TOT[\cdot]_{\mathrm{gs}} = 0$, and $TOT[\cdot]_0 = TOT[\cdot]_{\mathrm{eq}}$. The computation of the equilibrium state is a root finding problem for the nonlinear, F(). We use the Newton-Raphson method [39] to find the root, the set of the component activities in the equilibrium state. Let *F*: $\mathbb{R}^{\mathrm{n}} \rightarrow \mathbb{R}^{\mathrm{n}}$

Table 5. Table for the equilibrium computation.

	H_2O	H^+	$H_2CO_3^*$	H_4SiO_4	Al^{3+}	Ca^{2+}	Reaction	log K_{eq}	z	D (10^{-10} m^2/s)	Molar mass
1. H_2O	1	0	0	0	0	0	-	0.0	0	-	18.0152
2. H^+	0	1	0	0	0	0	-	0.0	+1	93.1	1.0079
3. $H_2CO_3^*$	0	0	1	0	0	0	-	0.0	0	19.2	62.0252
4. H_4SiO_4	0	0	0	1	0	0	-	0.0	0	17.0	96.1152
5. Al^{3+}	0	0	0	0	1	0	-	0.0	+3	5.59	26.9815
6. Ca^{2+}	0	0	0	0	0	1	-	0.0	+2	7.93	40.080
7. OH^-	1	-1	0	0	0	0	$H_2O - H^+ \Leftrightarrow OH^-$	-13.2	-1	52.7	17.0073
8. HCO_3^-	0	-1	1	0	0	0	$H_2CO_3^* - H^+ \Leftrightarrow HCO_3^-$	-6.15	-1	11.8	61.0173
9. CO_3^{2-}	0	-2	1	0	0	0	$H_2CO_3^* - 2H^+ \Leftrightarrow CO_3^{2-}$	-16.15	-2	9.65	60.0094
10. $H_3SiO_4^-$	0	-1	0	1	0	0	$H_4SiO_4 - H^+ \Leftrightarrow H_3SiO_4^-$	-9.2	-1	12	95.1073
11. $H_2SiO_4^{2-}$	0	-2	0	1	0	0	$H_4SiO_4 - 2H^+ \Leftrightarrow H_2SiO_4^{2-}$	-21.6	-2	8	94.0994
12. $Al(OH)^{++}$	1	-1	0	0	1	0	$Al^{3+} + H_2O - H^+ \Leftrightarrow Al(OH)^{++}$	-4.44	+2	8	43.9888
13. $Al(OH)_2^+$	2	-2	0	0	1	0	$Al^{3+} + 2H_2O - 2H^+ \Leftrightarrow Al(OH)_2^+$	-7.5	+1	12	60.9961
14. $Al(OH)_3$	3	-3	0	0	1	0	$Al^{3+} + 3H_2O - 3H^+ \Leftrightarrow Al(OH)_3$	-12.3	0	15	78.0034
15. $Al(OH)_4^-$	4	-4	0	0	1	0	$Al^{3+} + 4H_2O - 4H^+ \Leftrightarrow Al(OH)_4^-$	-19.6	-1	10	95.0107

and $x_k \in R^n$ be the k-th approximation for the root. The next approximation is estimated as $x_{k+1} = x_k - {J_{x_k}}^{-1} F(x_k)$ where J_{x_n} is the Jacobian matrix at x_k.

There is another way to compute the equilibrium state. In Table 5, H^+ is the only component coupled with all the secondary species, but the other components are not directly coupled with each other. Therefore, we can compute the other component activities from the estimated $\{H^+\}_{gs}$ and the total concentrations, $TOT[\cdot]_0$. For example, consider the total concentration of $H_2CO_3^*$ and the corresponding species, $H_2CO_3^*$, HCO_3^-, and CO_3^{2-}. The equation for the total concentration of $H_2CO_3^*$ is rewritten to obtain $\{H_2CO_3^*\}$,

$$\begin{aligned} TOT[\mathrm{H_2CO_3^*}]_0 &= [\mathrm{H_2CO_3^*}] + [\mathrm{HCO_3^-}] + [\mathrm{CO_3^{2-}}] \\ &= \frac{\{\mathrm{H_2CO_3^*}\}}{\gamma_{\mathrm{H_2CO_3^*}}} + \frac{\{\mathrm{HCO_3^-}\}}{\gamma_{\mathrm{HCO_3^-}}} + \frac{\{\mathrm{CO_3^{2-}}\}}{\gamma_{\mathrm{CO_3^{2-}}}} \\ &= \frac{\{\mathrm{H_2CO_3^*}\}}{\gamma_{\mathrm{H_2CO_3^*}}} + \frac{\mathrm{K_2}\{\mathrm{H_2CO_3^*}\}\{\mathrm{H^+}\}^{-1}}{\gamma_{\mathrm{HCO_3^-}}} + \frac{\mathrm{K_3}\{\mathrm{H_2CO_3^*}\}\{\mathrm{H^+}\}^{-2}}{\gamma_{\mathrm{CO_3^{2-}}}} \\ &= \{\mathrm{H_2CO_3^*}\}\left(\frac{1}{\gamma_{\mathrm{H_2CO_3^*}}} + \frac{\mathrm{K_2}\{\mathrm{H^+}\}^{-1}}{\gamma_{\mathrm{HCO_3^-}}} + \frac{\mathrm{K_3}\{\mathrm{H^+}\}^{-2}}{\gamma_{\mathrm{CO_3^{2-}}}}\right). \end{aligned} \tag{22}$$

Thus,

$$\{\mathrm{H_2CO_3^*}\} = TOT[\mathrm{H_2CO_3^*}]_0 \left(\frac{1}{\gamma_{\mathrm{H_2CO_3^*}}} + \frac{\mathrm{K_2}\{\mathrm{H^+}\}^{-1}}{\gamma_{\mathrm{HCO_3^-}}} + \frac{\mathrm{K_3}\{\mathrm{H^+}\}^{-2}}{\gamma_{\mathrm{CO_3^{2-}}}}\right)^{-1}. \tag{23}$$

From (23), $\{H_2CO_3^*\}$ is determined by the $\{H^+\}$ and $TOT[H_2CO_3^*]_0$. Moreover, $\{H_2CO_3^*\}$ obtained by (23) satisfies the conservation of $TOT[H_2CO_3^*]$. The activities of the other components are computed analogously:

$$\{\mathrm{H_4SiO_4}\} = TOT[\mathrm{H_4SiO_4}]_0 \left(\frac{1}{\gamma_{\mathrm{H_4SiO_4}}} + \frac{\mathrm{K_4}\{\mathrm{H^+}\}^{-1}}{\gamma_{\mathrm{H_3SiO_4^-}}} + \frac{\mathrm{K_5}\{\mathrm{H^+}\}^{-2}}{\gamma_{\mathrm{H_2SiO_4^{2-}}}} \right)^{-1}, \tag{24}$$

$$\{\mathrm{Al^{3+}}\} = TOT[\mathrm{Al^{3+}}]_0 \left(\frac{1}{\gamma_{\mathrm{Al^{3+}}}} + \frac{\mathrm{K_6}\{\mathrm{H^+}\}^{-1}}{\gamma_{\mathrm{Al(OH)^{++}}}} + \frac{\mathrm{K_7}\{\mathrm{H^+}\}^{-2}}{\gamma_{\mathrm{Al(OH)_2^+}}} + \frac{\mathrm{K_8}\{\mathrm{H^+}\}^{-3}}{\gamma_{\mathrm{Al(OH)_3}}} + \frac{\mathrm{K_9}\{\mathrm{H^+}\}^{-4}}{\gamma_{\mathrm{Al(OH)_4^{-1}}}} \right)^{-1}, \tag{25}$$

$$\{\mathrm{Ca^{2+}}\} = TOT[\mathrm{Ca^{2+}}]_0 \gamma_{\mathrm{Ca^{2+}}}. \tag{26}$$

From (23)–(26), we have all the component activities which satisfy the conservation of $TOT[\mathrm{H_2CO_3^*}]$, $TOT[\mathrm{H_4SiO_4}]$, $TOT[\mathrm{Al^{3+}}]$, $TOT[\mathrm{Ca^{2+}}]$, and $TOT[\mathrm{H_2O}]$ when $\{\mathrm{H^+}\}$ is given. The only condition not enforced is the conservation of $TOT[\mathrm{H^+}]$. For a given $\{\mathrm{H^+}\}_{gs}$, we derive the activities of the other components by (23)–(26), and compute $TOT[\mathrm{H^+}]_{gs}$ and $\Delta TOT[\mathrm{H^+}]$. Thus, the problem of the equilibrium computation is how to find $\{\mathrm{H^+}\}$ to satisfy $\Delta TOT[\mathrm{H^+}] = 0$, i.e., $TOT[\mathrm{H^+}]=TOT[\mathrm{H^+}]_0$. We express the above procedure by a function, f:$\mathbb{R}\rightarrow\mathbb{R}$ such that f($[\mathrm{H^+}]_{gs}$)=($\Delta TOT[\mathrm{H^+}]$) and f($[\mathrm{H^+}]_{eq}$) = 0. We can use the secant method to find the root of f( ).

This new method is simpler and faster than the previous method because it simplifies the equilibrium computation to a 1D root finding. The new method uses the simplicity of the system of the reactions, but it cannot be used for a general system of chemical reactions. For example, if there is a reaction which has both $\mathrm{H_2CO_3^*}$ and $\mathrm{H_4SiO_4}$ together, the new method cannot be applied.

c. Initial and boundary conditions

The domain of the simulation is the pore space of a rock. Acidic saline water with CO_2 dissolved is injected into the computational domain via top boundary at fixed pressure. The amount of CO2 dissolved in the inflowing water is calculated by the method as in Section II.4.d. [4, 40]. The concentration, $[H_2CO_3^*]$, of the injected solution is the CO_2 solubility. The inflow is assumed to be an equilibrium state of the 9 instantaneous reactions with the computed $[H_2CO_3^*]$. There are no silica-bearing or aluminum-bearing species in the injected solution. Ca^{2+} is added to the injected solution by the equilibrium of the saline water with quartz and kaolinite; $[Ca^{2+}] = 7.9\times10^{-6}$ M in the injected solution. The saline water has the total dissolved solutes (TDS) of 0.45 M. Thus, $[Na^+] = [Cl^-] = 0.45$ M [4].

The outlet in the simulation is the bottom boundary. The side boundaries are sealed to flow.

Initially, the pore space of the rock is filled with saline water, and the water is in equilibrium relative to the 9 instantaneous reactions. As with the injected fluid, $[Ca^{2+}] = 7.9\times10^{-6}$ M, and $[Na^+] = [Cl^-] = 0.45$ M [4].

d. CO_2 solubility in aqueous NaCl solution

In our simulations, the injected fluid has a concentration of dissolved CO_2 and a method to predict the amount of dissolved CO_2 is introduced [40]. CO_2 solubility is determined from the balance between the chemical potential $\mu^l_{CO_2}$ of CO_2 in the liquid phase and its potential $\mu^v_{CO_2}$ in the gas phase. At equilibrium, $\mu^l_{CO_2} = \mu^v_{CO_2}$, and the expansion of excess Gibbs energy is applied [40].

$$\ln\frac{y_{CO_2}P}{m_{CO_2}} = \frac{\mu_{CO_2}^{l(0)}}{RT} - \ln\phi_{CO_2}(T,P,y) + \sum_c 2\lambda_{CO_2-c}m_c + \sum_a 2\lambda_{CO_2-a}m_a + \sum_c\sum_a \zeta_{CO_2-c-a}m_c m_a\,, \tag{27}$$

where the subscript, 'c' represents cation and 'a' represents anion. The CO_2 fractional vapor pressure, y_{CO_2}, is computed by

$$y_{CO_2} = \frac{P - P_{H_2O}}{P}, \tag{28}$$

where the pure water pressure, P_{H_2O} is estimated by

$$P_{H_2O} = \frac{P_c T}{T_c}[1 + b_1(-t)^{1.9} + b_2 t + b_3 t^2 + b_4 t^3 + b_5 t^4]. \tag{29}$$

Here $t = \frac{T-T_c}{T_c}$, and the critical pressure, P_c, and critical temperature, T_c, are 220.85 bar and 647.29 K respectively. $\frac{\mu_{CO_2}^{l(0)}}{RT}$, λ_{CO_2}, and ζ_{CO_2} are estimated by

$$X(T,P) = c_1 + c_2 T + \frac{c_3}{T} + c_4 T^2 + \frac{c_5}{630-T} + c_6 P + c_7 P\,ln\,T + c_8\frac{P}{T} + c_9\frac{P}{630-T} + \frac{c_{10}P^2}{(630-T)^2}\,. \tag{30}$$

The fugacity coefficient of CO_2, $ln\,\phi\,(T,P)$ is computed by

$$ln\,\phi(T,P) = Z - 1 - ln\,Z + \frac{a_1 + \frac{a_2}{T_r^2} + \frac{a_3}{T_r^3}}{V_r} + \frac{a_4 + \frac{a_5}{T_r^2} + \frac{a_6}{T_r^3}}{2V_r}$$
$$+ \frac{a_7 + \frac{a_8}{T_r^2} + \frac{a_9}{T_r^3}}{4V_r} + \frac{a_{10} + \frac{a_{11}}{T_r^2} + \frac{a_{12}}{T_r^3}}{5V_r} \quad (31)$$
$$+ \frac{a_{13}}{2T_r^3 a_{15}}\left[a_{14} + 1 - \left(a_{14} + 1 + \frac{a_{15}}{V_r^2}\right) exp\left(-\frac{a_{15}}{V_r^2}\right)\right],$$

where

$$Z = \frac{P_r V_r}{T_r} = 1 + \frac{a_1 + \frac{a_2}{T_r^2} + \frac{a_3}{T_r^3}}{V_r} + \frac{a_4 + \frac{a_5}{T_r^2} + \frac{a_6}{T_r^3}}{V_r^2} + \frac{a_7 + \frac{a_8}{T_r^2} + \frac{a_9}{T_r^3}}{V_r^4}$$
$$+ \frac{a_{10} + \frac{a_{11}}{T_r^2} + \frac{a_{12}}{T_r^3}}{V_r^5} + \frac{a_{13}}{T_r^3 V_r^2}\left(a_{14} + \frac{a_{15}}{V_r^2}\right) exp\left(-\frac{a_{15}}{V_r^2}\right). \quad (32)$$

Here,

$$P_r = \frac{P}{P_c}, \qquad T_r = \frac{T}{T_c}, \qquad V_r = \frac{V}{V_c}.$$

The critical pressure, P_c=220.85 bar and the critical temperature, T_c=647.29 K. V_c is defined by

$$V_c = \frac{RT_c}{P_c}. \quad (33)$$

R is the universal gas constant, and R=8.314467 Pa m^3/K·mol. All coefficients, a_i's, b_i's,

and c_i's are listed in [40].

e. Activity coefficients and diffusion coefficients

The activity is different from the concentration and it is the real effective reactivity of a species [37]. The activity coefficient is the ratio of the activity to the concentration of the species,

$$\gamma = \frac{\{\cdot\}}{[\cdot]}. \tag{34}$$

The activity coefficients of aqueous species can be estimated by the Davis' equation [37]. Define the ionic strength, I, as

$$I = \frac{1}{2}\sum_i \mathrm{m}_i \mathrm{z}_i^2 , \tag{35}$$

where m_i is the molar concentration of species i in M (mol/liter) and z_i is the ionic charge of the species i. The activity coefficient, γ is computed by Davis' equation for $I < 0.5$ M by

$$\log\gamma = -\mathrm{A}\mathrm{z}^2\left(\frac{I^{1/2}}{1.0 + I^{1/2}} - 0.2I\right), \tag{36}$$

where $\mathrm{A} = 1.82 \times 10^6(\varepsilon\mathrm{T})^{-3/2}$ and ε is the dielectric constant. A = 0.51 for water at 25 ^{o}C. Table 6 gives the values of ε for other temperatures in order to compute A at other temperature values [41].

The water activity is close to 1.0 under moderate conditions, and the water activity of dimensionless 1.0 is accurate enough for many analyses in water chemistry. The water activity and water concentration is 1.0 and 54.7M respectively in the simulation. There are only 4 unknown activities/concentrations out of 6 components in the equilibrium computation since H_2O and Ca^{2+} are not variables in the equilibrium computation.

Table 6. Table of temperature vs. dielectric constant of pure water [41].

T	ε
0°C	87.7
25°C	78.3
50°C	69.9
100°C	55.7

Equation (11) has a diffusion term, $\sum_j D_{[\cdot]} a_{ij} \frac{[\cdot]_j - [\cdot]_i}{l_{ij}}$. Thus, the diffusion coefficients of all species are needed. The values of the diffusion coefficients at T = 25 °C and P = 101.3 kPa are listed in Table 5 [41, 42]. The diffusion coefficients are adjusted to those under the simulation condition, T = 50°C and P = 100 bar by the Stokes-Einstein relation [41],

$$D_{T_1} \times \mu_{w,T_1} T_1 = D_{T_2} \times \mu_{w,T_2} T_2 \,. \tag{37}$$

In (37), T_1 and T_2 are two given temperatures, D_{T_1} and D_{T_2} are the diffusion coefficients at T_1 and T_2, and μ_{w,T_1} and μ_{w,T_2} are water viscosities at T_1 and T_2.

f. Effective and volume-averaged reaction rates [4]

From the network flow model, the bulk mass change rates (*mol/s*) of anorthite and kaolinite can be defined by the sum of the mass change rate of all pores:

$$M_A = \sum_{i=1} A_{A,i} r_{A,i} \,, \qquad M_K = \sum_{i=1} A_{K,i} r_{K,i} \,. \tag{38}$$

The subscripts, *A* and *K* represent anorthite and kaolinite respectively; the subscript *i* is the pore index; *A* and *r* are the mineral surface area and kinetic reaction rate of a pore. The effective reaction rates ($mol/m^2 s$) are defined by

$$R_{N,A} = \frac{\sum_{i=1} A_{A,i} r_{A,i}}{\sum_{i=1} A_{A,i}}, \qquad R_{N,K} = \frac{\sum_{i=1} A_{K,i} r_{K,i}}{\sum_{i=1} A_{K,i}}. \tag{39}$$

Thus, the effective reaction rates include reaction rates in all pores – pore scale heterogeneities in reaction rates.

The volume-averaged concentration of a species is defined by

$$\overline{[\cdot]} = \frac{\sum_{i=1}[\cdot]_i V_i}{\sum_{i=1} V_i}. \tag{40}$$

The volume-averaged activity can be defined from the volume-averaged concentrations by $\overline{[\cdot]} = \gamma_{\overline{[\cdot]}}\overline{\{\cdot\}}$. Thus for the anorthite and kaolinite reactions, the volume-averaged reaction rates analogous to (12) and (14) can be defined using volume-averaged activities:

$$\begin{aligned} \overline{R_A} &= \left(k_H \overline{\{H^+\}}^{1.5} + k_{H_2O} + k_{OH}\overline{\{OH^-\}}^{0.33}\right)(1 - \overline{\Omega_A}), \\ \overline{R_K} &= \left(k_H \overline{\{H^+\}}^{0.4} + k_{OH}\overline{\{OH^+\}}^{0.3}\right)\left(1 - \overline{\Omega_K}^{0.9}\right). \end{aligned} \tag{41}$$

Here, $\overline{\Omega_A}$ and $\overline{\Omega_K}$ are the volume-averaged saturation states from (13) and (15) using the volume-averaged activities. Define the ratio of the two reaction rates,

$$\beta_A = \frac{\overline{R_A}}{R_{N,A}}, \qquad \beta_K = \frac{\overline{R_K}}{R_{N,K}}. \tag{42}$$

III. Computational results

1. Mineral distributions

Ideally, segmentation of selected mineral should utilize knowledge of the CT values (attenuation coefficients) for each mineral [43]. The uncertainty in X-ray attenuation values due to partial voxel effects, impurities, beam energy width/hardening, and detection instrument drift create a "detection spread" complicating the segmentation. The CT values in our reconstructed images, which vary with X-ray energy, have not been correlated to mineral type, so in this preliminary "proof of concept" work, segmentations are visually guided and validation is accomplished using comparison to the BSE/EDX analysis of Peters[19].

As the reconstructed tomographic images indicate, visual identification of air and MoI phases is fairly robust. Distinction between quartz and kaolinite is somewhat more problematic within the pore space. Histograms of the CT values are shown in Fig. 8. Material and air phases are visible as two peaks in Viking14W5, and as a peak and a shoulder in Viking3W4. In Viking10W4, no air peak is visible. This correlates with the relative porosity values of the three samples. Individual mineral phases do not appear as separate peaks due to the "detection spread" noted above. Table 7 indicates the T_0 and T_1 threshold CT values ultimately chosen for each bi-phase segmentation. These threshold values are also indicated in Fig. 8 as "windows", with the LHS of the window corresponding to T_0 and the RHS to T_1.

Table 7. Threshholds, T_0 and T_1 for bi-phase segmentations.

	Void	kaolinite	quartz	MoI
Sandstone	15150 - 15800	15950 - 16500	18100 - 18700	
Shaly sandstone	9150 - 9750	9900 - 10500	12550 - 13150	
Conglomerate sandstone	7700 - 8200	8400 - 9350	11250 - 11950	

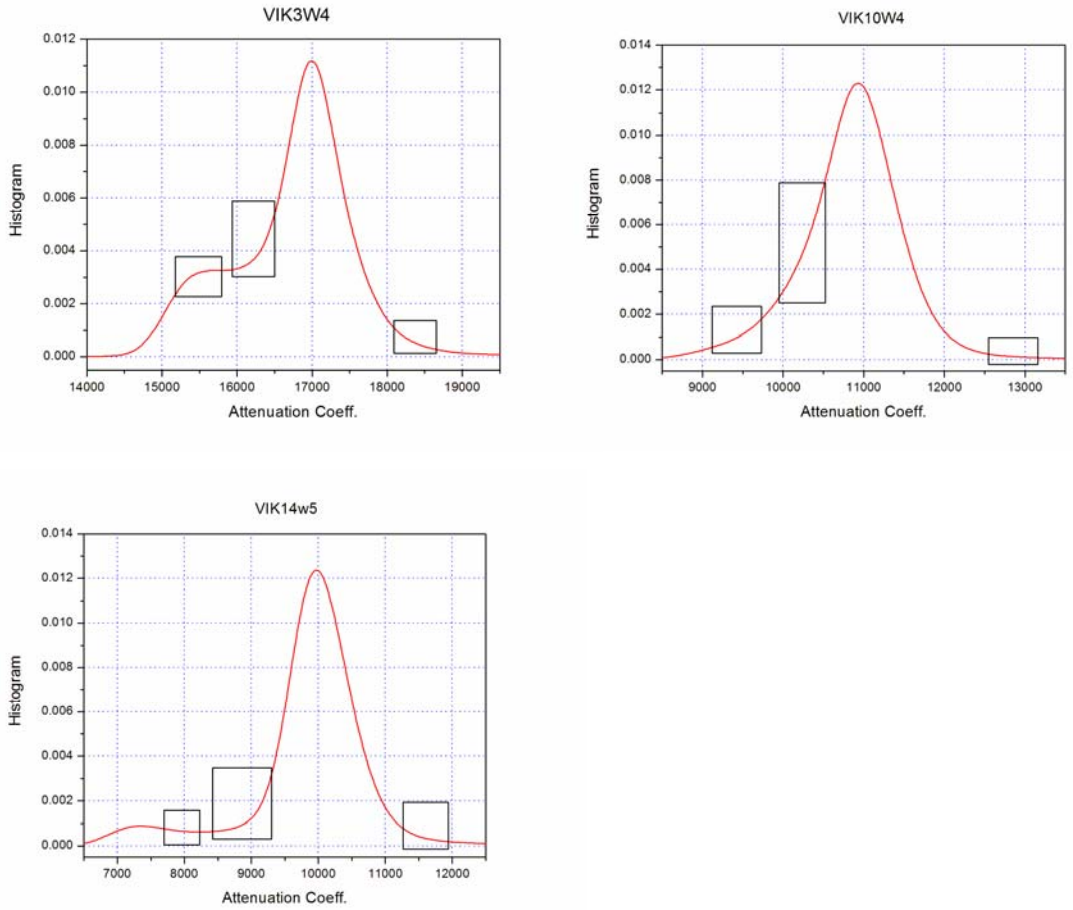

Fig. 8. Histograms of the attenuation coefficients of three Viking samples with the threshold windows.

Fig. 9 (a), (b), (c), and (d) illustrate, using one of the slices from Viking14W5, the results of the three bi-phase segmentation steps that produce the final four-phase segmentation. Fig. 9 (e) shows the final four-phase segmentation after adjustment of the inter-phase surface as explained in II.2.c. Visual comparison of Fig. 9 (a) and (e) provides a qualitative assessment of the segmentation. Fig. 10 and Fig. 11 show the four-phase segmentations for Viking3W4 and Viking10W4.

As explained in Section II.2.c, surface areas are corrected by the specific surface area, S/V = 40,000 cm^{-1} from BET measurement; the correction factors for the sandstone, the shaly sandstone, and the conglomerate sandstone are 41.7, 34.2, and 61.5 respectively.

To validate the segmentation, mineral abundances and accessibilities were computed and compared to the values obtained from the BSE analysis of Peters [19]. Mineral abundance is defined as the ratio of total mineral volume to total grain volume, and mineral accessibility is defined as the ratio of total surface area between the mineral and void space to total surface area between grain and void space. The comparisons are given in Table 8. Values from the CT analysis are given before and after the inter-phase surface adjustment to quantify the impact of that correction. The median correction is 0.45%; the worst case results in a 2% change. In addition to segmentation errors, differences between the CT and BSE measure values can be attributed to the following. i) The CMT results are 3-dimensional, while the BSE results are based upon 2-dimensional surface measurements. ii) Only small regions are investigated (the BSE results are based upon a sample of a different surface locations), and come from different places on a larger core sample. iii) Detection resolutions are different; CMT voxel sizes are 3.98 μm while BSE pixel sizes are 1.8 μm.

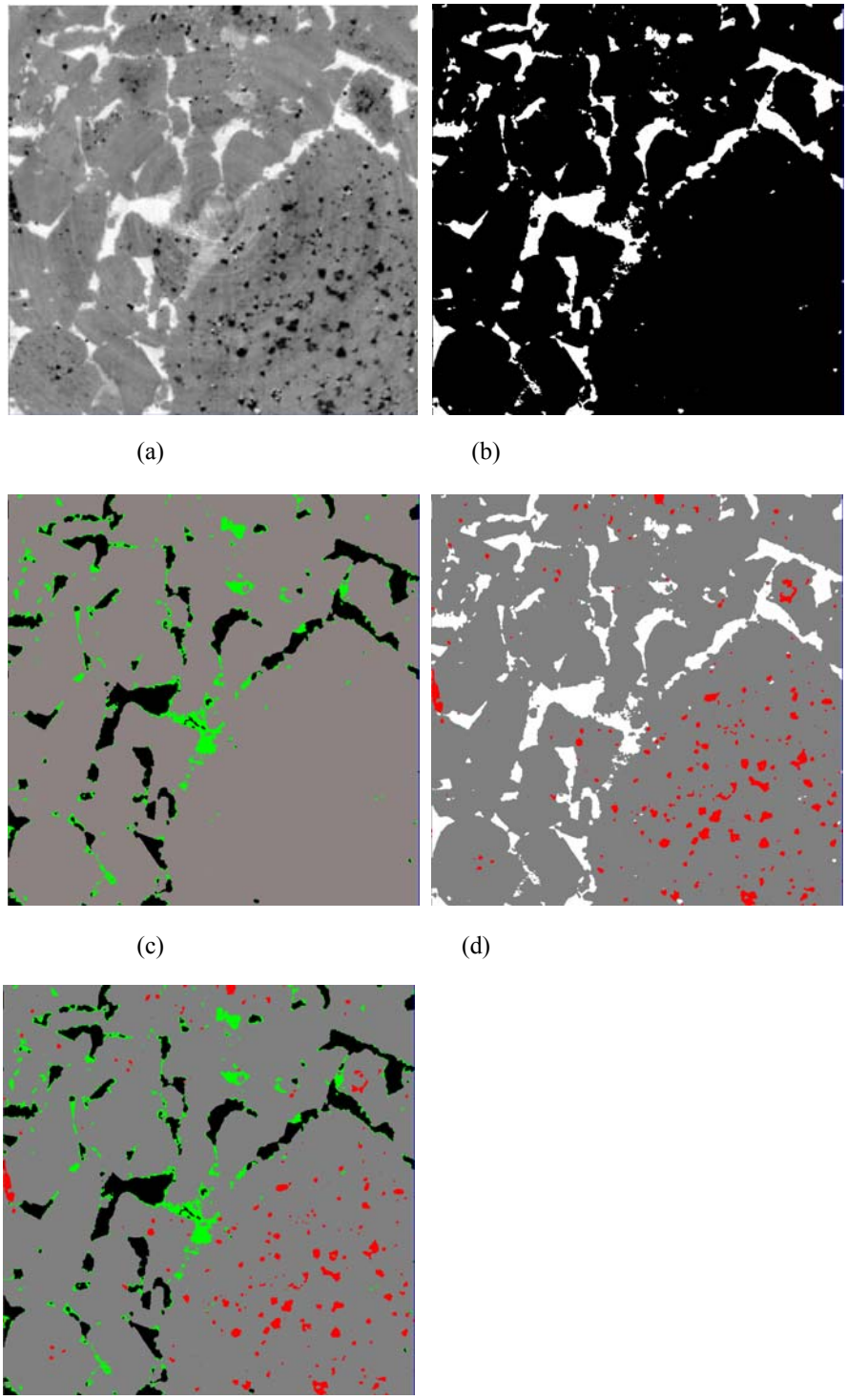

(a) (b)

(c) (d)

(e)

Fig. 9. (a) One slice of grey scale image of the conglomerate sandstone (Viking14W5). (b)

Bi-phase segmented image of the primary pore and primary grain spaces. Black and white indicate the primary grain and primary pore respectively. (c) Segmented image of void and kaolinite in the primary pore space. Black and green indicate void and kaolinite respectively. Grey indicates the primary grain space. (d) Segmented image of quartz and MoI. Grey and red indicate quartz and MoI respectively. White indicates the primary pore space. (e) The final four-phase segmented image. Black, green, grey, and red indicate void, kaolinite, quartz, and MoI respectively.

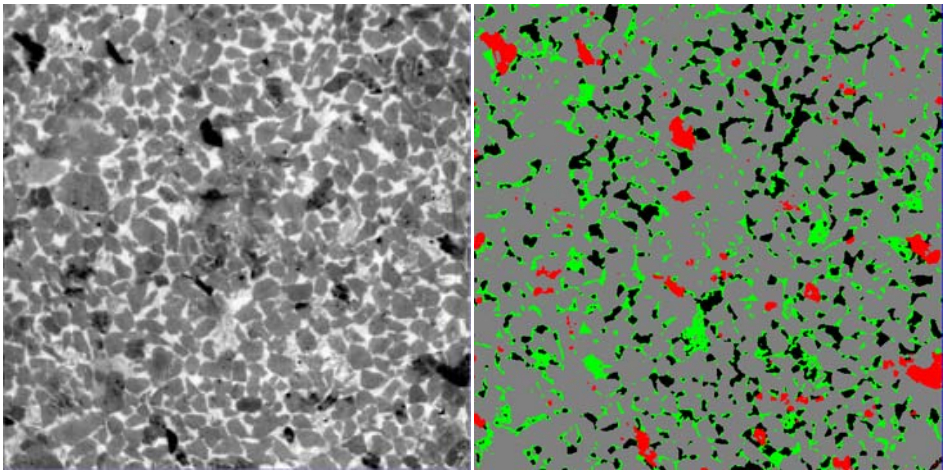

Fig. 10. Grey scale and four-phase segmented images of the sandstone (Viking3W4).

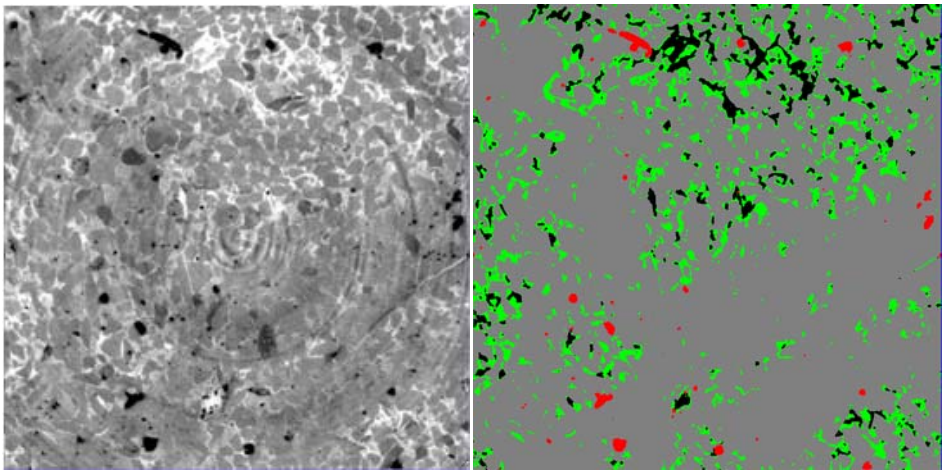

Fig. 11. Grey scale and four-phase segmented images of the shaly sandstone (Viking10W4).

Table 8. Mineral abundances and accessibilities of three Viking samples. The abundances and accessibilities are compared with those by BSE analysis [19].

		Porosity	Mineral abundances(%)			Mineral accessibilities(%)		
			kaoli.	quartz	MoI	kaoli.	quartz	MoI
Sandstone	BSE	18	21	73	6	81	17	2
	CMT	13	14	84	2	64.1	35.8	0.06
	CMT corrected	14	15	82	3	63.4	35.3	1.3
Shaly sandstone	BSE	7	31	64	5	86	13	1
	CMT	4	10	89	1	70.2	29.8	0.03
	CMT corrected	4	10	89	1	69.8	29.5	0.7
Congl. sandstone	BSE	8	5	94	1	65	35	<1
	CMT	7	3	95	2	52.8	47.0	0.2
	CT corrected	7	3	95	2	52.3	46.4	1.3

Fig. 12 presents pore volume, throat area, coordination number and medial axis (channel) length distributions determined from the pore-throat network of the primary pore space for the three samples. As is typical for well-sorted sandstones [15], the volume distribution for Viking3W4 and Viking10W4 is log-normal. The distribution for the conglomerate sandstone, Viking14W5 is bi-normal, indicative of its composition from grains that are poorly-sorted. Throat area and channel length distributions are correspondingly different for Viking14W5 than for the other two. Throat areas tend to peak smaller but have a larger “tail” of large sized throats. Channel lengths also have a large “tail” of longer channels. Interestingly, there are no appreciable differences in pore coordination numbers.

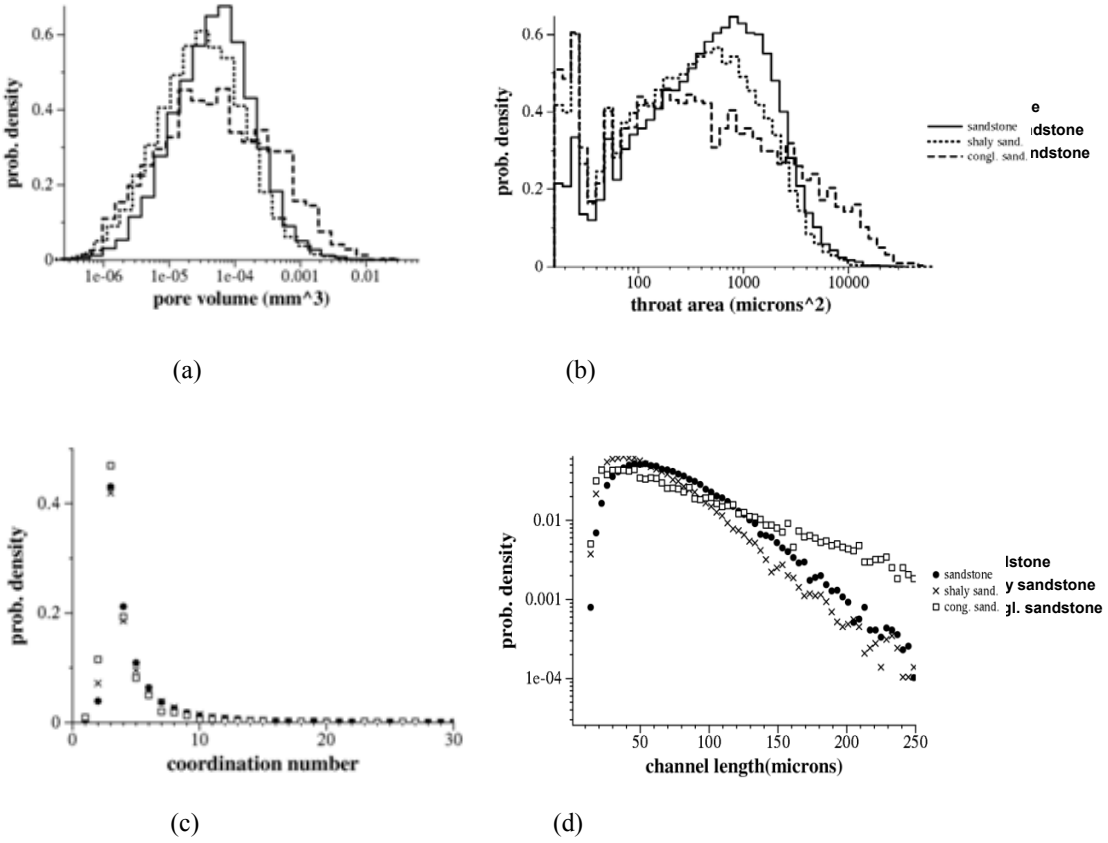

Fig. 12. Distributions of (a) pore volume, (b) throat area, (c) coordination number, and (d) channel length of the pore-throats networks for the three Viking samples. The sandstone data are represented by solid lines and '•'. The shaly sandstone data are represented by dotted lines and 'x'. The conglomerate sandstone data are represented by dashed lines and '□'.

Table 9. The numbers of pores which contain kaolinite or are in contact with MoI.

	sandstone	Shaly sandstone	Congl. sandstone
Number of pores	14589	11040	1971
Number of pores of kaol.	14579 (99.9 %)	11037 (100 %)	1969 (99.9 %)
Number of pores of MoI	2855 (20 %)	655 (6 %)	464 (24 %)

Table 9 details the numbers of primary pores that contain kaolinite or are in contact with MoI. Less than 25% of the pores in any sample type are in contact with MoI while over 99% of the pores contain kaolinite.

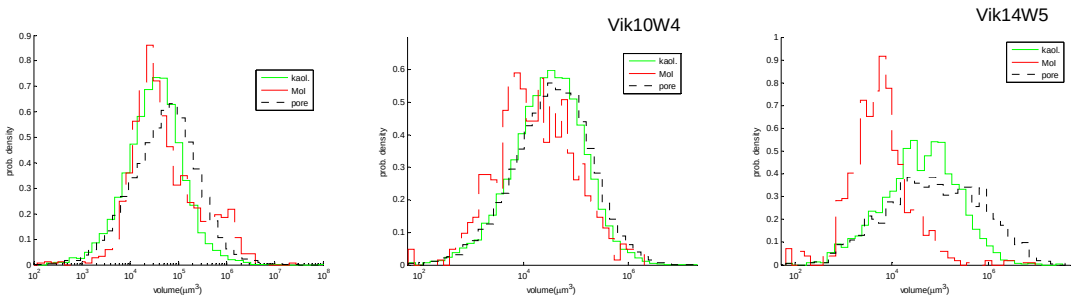

(a) (b) (c)

Fig. 13. Pore, kaolinite, and MoI volume distributions of (a) sandstone (Viking3W4), (b) shaly sandstone (Viking10W4), and (c) conglomerate sandstone (Viking14W5).

Fig. 13 presents the measured distribution of volumes of kaolinite and MoI. Since the kaolinite phase is distributed throughout the primary pore space, a kaolinite volume is restricted to the amount present in any single pore. The MoI phase is distributed in individual "grains", and each grain volume is represented in the distributions. As indicated from Table 9, and seen in Fig. 13, the kaolinite volume distribution will track the pore volume distribution very closely. In general, the MoI grain volumes are smaller than pore volumes. The largest difference is for the conglomerate sandstone. Table 10 presents statistics on average pore, kaolinite, and MoI grain volumes for the three samples.

Table 10. Average of volumes of pore, kaolinite, and MoI.

		Sandstone	Shaly sandstone	Conglomerate sandstone
Volume (μm^3)	Pore	1.99×10^5	1.43×10^5	6.39×10^5
	Kaolinite	9.45×10^4	1.01×10^5	1.72×10^5
	MoI	1.45×10^5	7.39×10^4	5.16×10^4
Surf. area (μm^2)	Pore	8.40×10^5	6.02×10^5	2.63×10^6
	Kaolinite, 1st	3.38×10^5	2.34×10^5	1.19×10^6
	Kaolinite, 2nd	5.91×10^5	5.14×10^5	1.58×10^6
	MoI	5.92×10^4	2.43×10^4	7.02×10^4

Fig. 14 presents the measured distribution of surface areas of the kaolinite and MoI phases and compares them to the primary pore surface area distribution. Again, as the kaolinite phase is distributed throughout the primary pore space, each segment of kaolinite phase under is that restricted to the amount present in any single pore. The MoI phase is distributed in individual "grains", and each grain surface area is represented in the distributions. With reference to Fig. 4, the MoI surface area is (S_{RG}+S_{RB}). The average surface areas are also presented in Table 10.

Consider a single pore, volume V_{pore}, as shown in Fig. 4 which contains kaolinite (of volume V_G), and is in contact with one or more "grains" of MoI phase (in Fig. 4 two grains of volume V_{R1} and V_{R2} are shown). We define the "kaolinite pore volume" for this pore as V_G/V_{pore}. As kaolinite is always found within the primary pore space, kaolinite pore volume varies between 0 and 1. The "MoI pore volume" for this pore is defined as $(V_{R1}+V_{R2})/V_{pore}$. Note that MoI pore volume can exceed a value of 1. Analogously, the

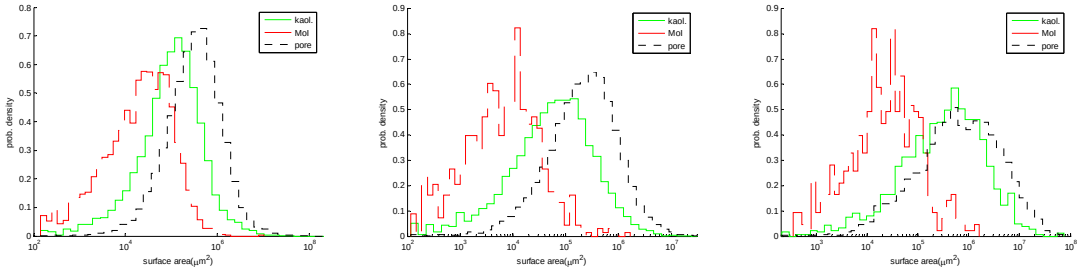

(a) (b) (c)

Fig. 14. Pore, 2nd kaolinite, and MoI surface area distributions of (a) sandstone, (b) shaly sandstone, and (c) conglomerate sandstone.

"MoI pore area" is defined as the surface area ratio $(S_{RG}+S_{RB})/S_{pore}$. There are two definable "kaolinite pore area" for a pore body, between the kaolinite and the void space S_{GB}/S_{pore}, and between the kaolinite and the primary grain phase $(S_{GQ}+S_{RG})/S_{pore}$. The first kaolinite pore area measure can exceed 1, but the second measure is bound between 0 and 1.

Fig. 15 presents the measured distributions for kaolinite and MoI pore volumes. These are just a recasting of the data presented in Fig. 13, but now quantifying differences relative to the primary pore volume distribution. As per Table 9 and Fig. 13, the kaolinite pore volume distribution is sharply peaked at a value of 100%, with a long tail to smaller

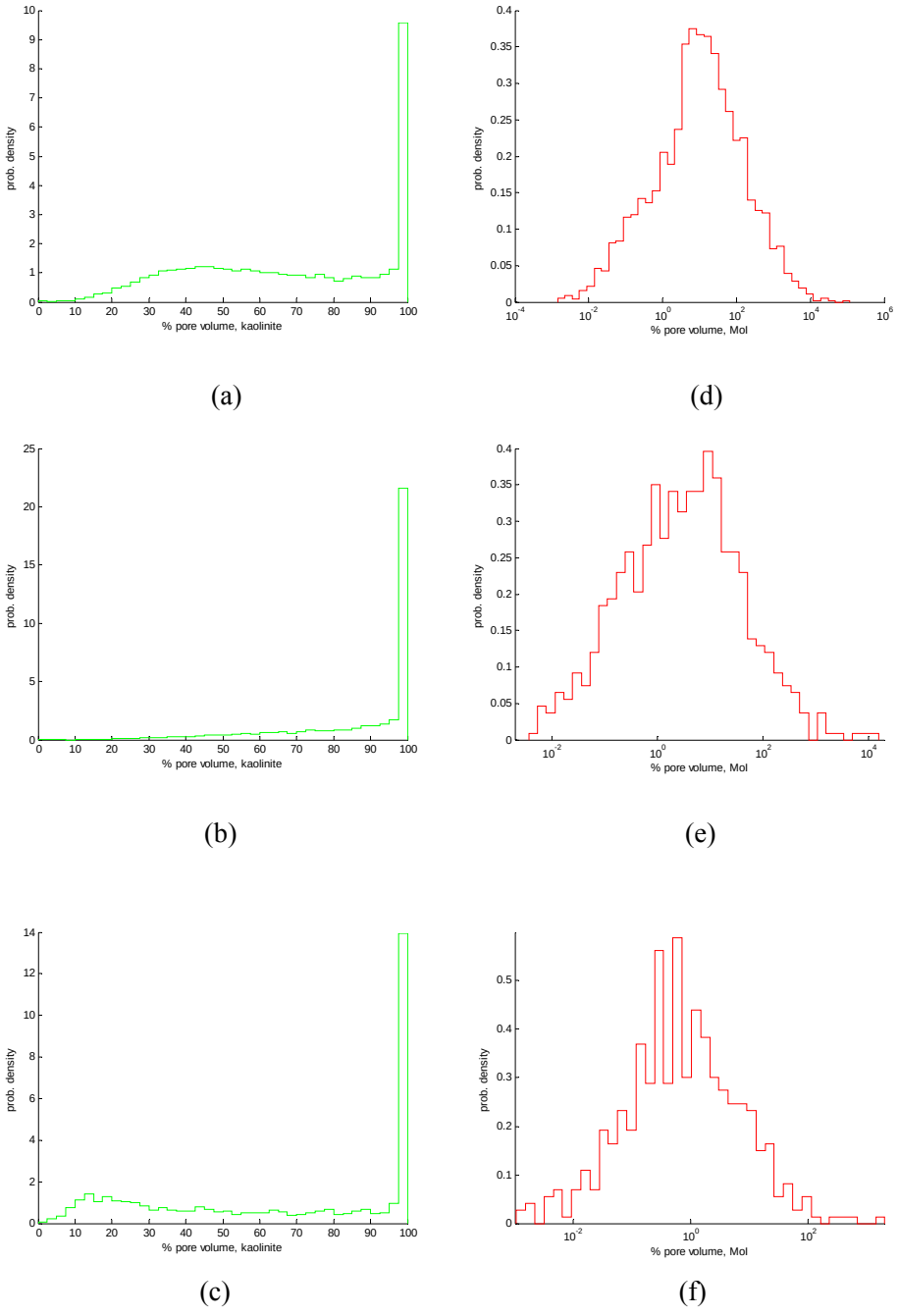

Fig. 15. Kaolinite pore volume distributions of (a) sandstone, (b) shaly sandstone, and (c) conglomerate sandstone. MoI pore volume distributions of (d) sandstone, (e) shaly sandstone, and (f) conglomerate sandstone.

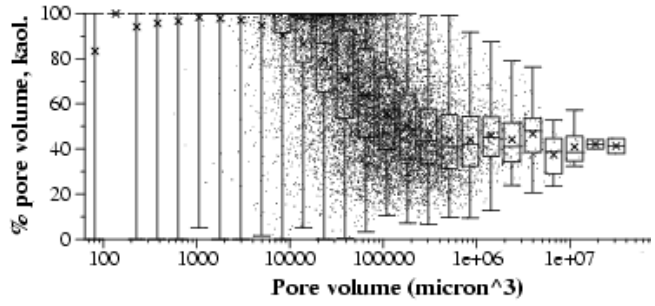

(a)

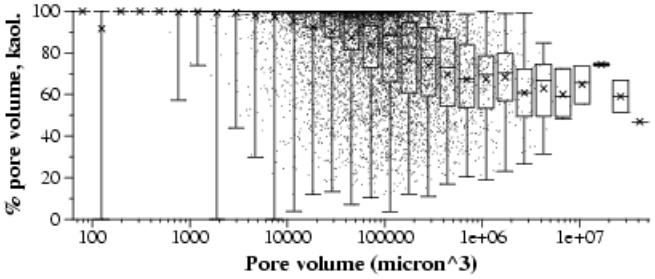

(b)

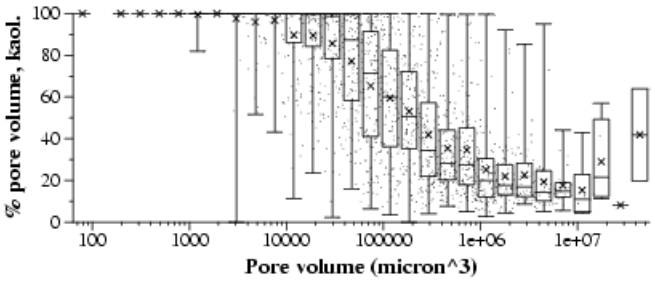

(c)

Fig. 16. Plots of kaolinite pore volume vs. pore volume, (a) sandstone, (b) shaly sandstone, and (c) conglomerate sandstone.

values. However, unlike Fig. 13 which measures individual MoI grains, the MoI pore volume distribution in Fig. 15 is peaked at or above a value of 100% as frequently two or more MoI grains are "in contact with" the same pore.

As kaolinite is highly correlated with primary pore, Fig. 16 presents a scatter plot showing kaolinite occupancy (measure as kaolinite pore volume) as a function of primary

pore volume. The data indicate that small pores are generally 100% full of kaolinite, with the occupancy dropping with pore size, tending to level off to a non-zero value (approximately 50% for the sandstone, 60% for shaly sandstone, and 20% for the conglomerate sandstone). These occupancy scatter plots are consistent with the migratory nature of the fine kaolinite grains occupancy of the pore space through fluid transport.

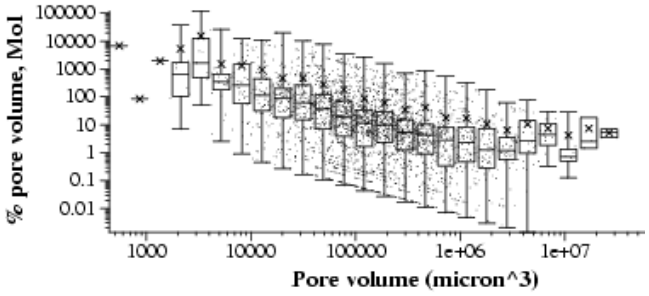

(a)

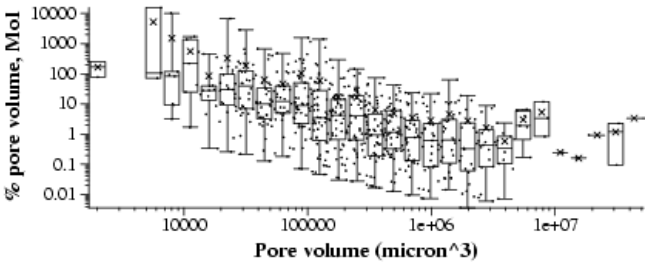

(b)

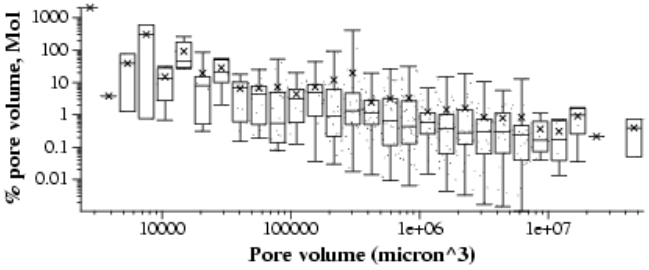

(c)

Fig. 17. Plots of MoI pore volume vs. pore volume, (a) sandstone, (b) shaly sandstone, and (c) conglomerate sandstone.

Analogous scatter plots of MoI pore volume versus primary pore volume are presented in Fig. 17. MoI pore volume decreases approximately linearly in log-log scale as pore volume increase. The slope is approximately -1. This correlation between MoI pore volume and pore volume is due to the change of pore volume which is the denominator in the MoI pore volume. Thus, the plot shows a weak correlation between the MoI volume and pore volume.

Fig. 18 presents the measured distributions for kaolinite and MoI pore areas. These are just a recasting of the data presented in Fig. 14, but now quantifying differences relative to the primary pore surface area distribution. The kaolinite pore area distribution is sharply peaked at a value of 100% due to its high occupancy in primary pores. Since MoI grains are uncorrelated with the primary pore space, the distribution has a peak associated with predominant MoI grain size. Again the data support the observation that typical MoI grains are smaller than typical primary pores.

Fig. 19 presents a scatter plot of the second kaolinite pore area versus pore surface area. The second kaolinite pore area shows a different distribution from the first; its peak occurs around 30% while a sharp peak at 100% for the first kaolinite pore area. The plot does not show any correlation between the second kaolinite pore area and pore surface area.

Fig. 20 presents a scatter plot of MoI pore area versus pore surface area. Like the plot in Fig. 17, Fig. 20 shows the similar correlation between MoI pore area and pore surface area. Similarly, the pore surface area, denominator in the definition of MoI pore area, results in this decreasing correlation and thus, this means no correlation between MoI surface area and pore surface area.

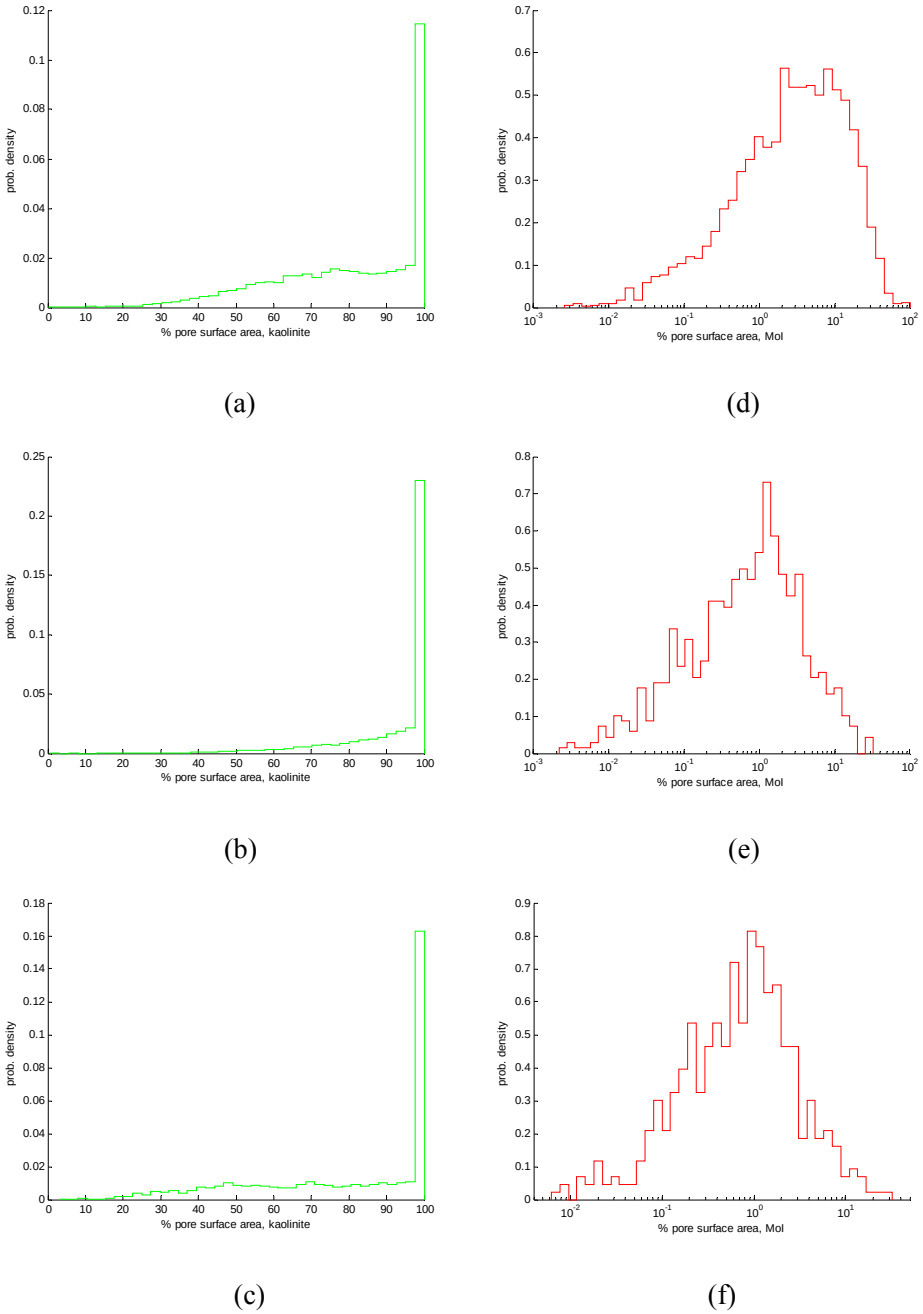

Fig. 18. Kaolinite pore area distributions of (a) sandstone, (b) shaly sandstone, and (c) conglomerate sandstone. MoI pore area of (d) sandstone, (e) shaly sandstone, and (f) conglomerate sandstone.

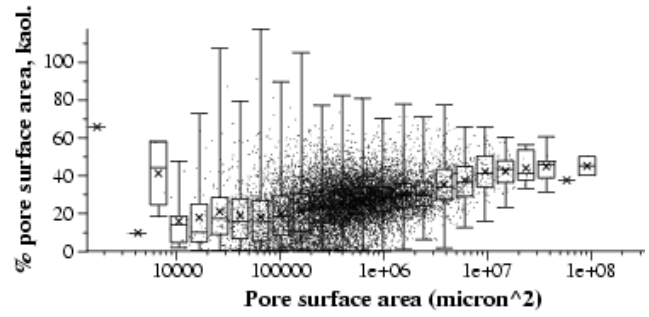

(a)

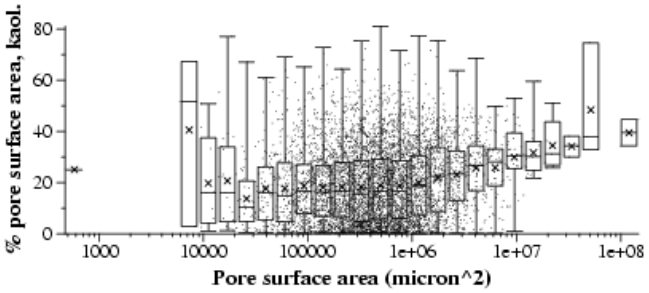

(b)

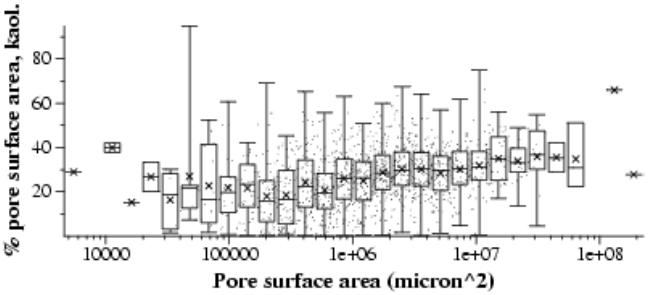

(c)

Fig. 19. Plots of kaolinite pore area vs. pore surface area, (a) sandstone, (b) shaly sandstone, and (c) conglomerate sandstone.

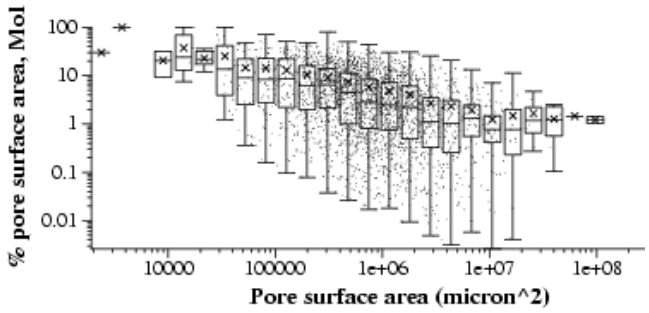

(a)

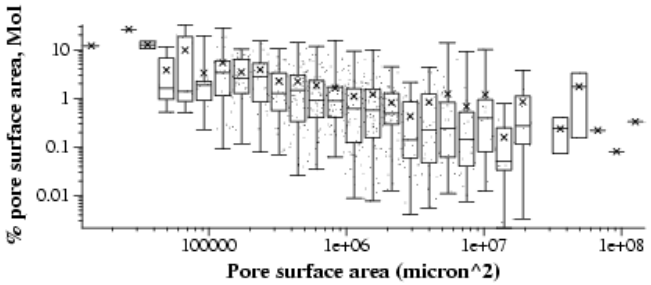

(b)

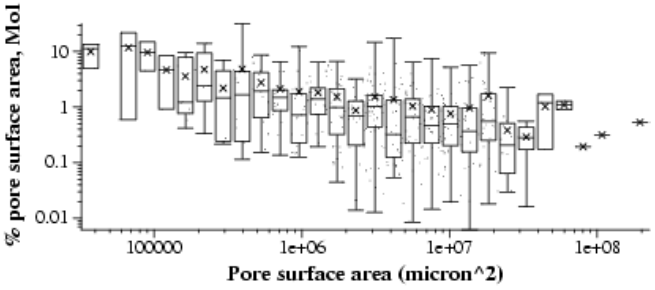

(c)

Fig. 20. Plots of MoI pore area vs. pore surface area, (a) sandstone, (b) shaly sandstone, and (c) conglomerate sandstone.

2. Simulation of reactive flows

a. Validation of the reactive models

The reactive network flow model was validated against published results [4]. An artificial sample is constructed as described below and the variables of the network are generated by random number generators following statistical distributions.

The sample size for the validation study is 5.0×1.7×5.0 mm^3 with a porosity of 14%. There are 9000 pores regularly distributed in 30×10×30 in the x-, y-, and z-directions respectively. Each interior pore is connected with six neighboring pores in the directions ±x, ±y, ±z. Pore volumes are generated based on the log-normal distribution with the log-mean, $\mu_{\log V} = -3.42$ and the log-standard deviation, $\sigma_{\log V} = 0.51$ in mm^3. The theoretical arithmetic mean of log-normal distribution is $e^{\mu+\frac{\sigma^2}{2}} = 7.6 \times 10^{-4} mm^3$ which makes the porosity approximately 16%. Thus, the all pore volumes are adjusted by multiplying a factor to ensure a porosity of 14%. Pore surface area follows the exponential distribution with $\mu_S = 6.0 mm^2$ with the restriction that the surface area generated exceeds $S_{min} = (4\pi)^{\frac{1}{3}}(3V)^{\frac{2}{3}}$ which is the spherical surface area from the pore volume.

For the channel conductances, the log of channel conductances, $X_{ij} = \log C_{ij}$ are generated by the joint Gaussian distribution with the sum, $Y_{ij} = \log V_i + \log V_j$ of log pore volumes of the two connected pores. The mean and standard deviation of Y_{ij} are $\mu_Y = 2\mu_{\log V}$ and $\sigma_Y = \sqrt{2}\sigma_{\log V}$, and the mean and standard deviation of X_{ij} are $\mu_X = -6.1$ and $\sigma_X = 1.0$ for the absolute permeability of 80md. For the log conductance, X_{ij} of each channel, the mean and standard deviation of X_{ij} of the channel is calculated by

$$\mu_{X,ij} = \mu_X + \rho\frac{\sigma_X}{\sigma_Y}\left(Y_{ij} - \mu_Y\right), \qquad \sigma^2_{X,ij} = \sigma^2_X(1-\rho^2). \tag{43}$$

Here, ρ is the correlation coefficient and ρ is 0.9 for (43). For each channel, $\mu_{X,ij}$ and $\sigma^2_{X,ij}$ are computed by the above equation, and X_{ij} of the channel is generated by the normal distribution random number generator. The channel conductance is then $C_{ij} = \mathrm{e}^{X_{ij}}$.

The channel cross section area is computed from the Poiseuille's flow through a circular pipe, which has the volume flow rate,

$$Q = \frac{\pi d^4}{128\mu}(-\nabla P). \tag{44}$$

The conductance is therefore

$$C = \frac{\pi d^4}{128\mu}. \tag{45}$$

From (45), the diameter and area of the cross section can be computed and the area is used as the channel cross section area. Channel length in any direction is constant. In the z-direction, channel length is computed by dividing the sample height by the number of channels in z. The channel lengths in the other directions are similarly computed.

A subset of 10% (900 pores) is selected to contain the reactive minerals, anorthite and kaolinite. The selection consists of blocks of pores. A block of 2×2×15 pores is

selected randomly in space and all 60 pores in the block are assigned as reactive pores. The 2×2×15 block is based upon typical feldspar grain sizes. There can be overlap between blocks. A few extra small blocks therefore generated to produce the required 900 pores. The surface area of each reactive pore is assumed to be half anorthite and half kaolinite. Since pore surface area is generated independently of pore volume, a few reactive pores can have extreme values of specific surface area. This results in a huge concentration change in the pore as a result of the anorthite and kaolinite reactions. This restricts the time step size used to solve the reaction kinetics. To avoid this problem, the volume of a pore having extremely large specific surface area is increased to a required minimum value. This process increases the overall porosity of the network by 0.01%. The specifics of the network generated are summarized in Table 11.

The initial and boundary conditions are computed as described in Section II.4.c. This simulation condition is same as the case A in Li's simulation [4]. The computed initial state is listed in Table 13, and its pH is 6.6. The solubility of CO_2 is 2.0 M giving an injected pH of 2.9. The three reactions and concentrations of the inflow are listed in Table 12 and Table 14 respectively. The flow rate of the injected water is computed from the average seepage velocity, $v_{seep} = 5.8 \times 10^{-3}$ cm/s. The volume flow rate, Q is computed by $Q = \phi A v_{seep} = 6.9 \times 10^{-11}$ m^3/s.

Table 11. Summary of the generated network.

Number of reactive pores		902
Pore volume (mm^3)	μ_V	6.611×10^{-4} mm^3
	$\mu_{\log V}$	-3.42
	$\sigma_{\log V}$	0.51
Mean of pore surface area		6.003 mm^2
Surface to volume ratio, S/V		9.081×10^{4} cm^{-1}
Porosity		14.01 %
Mean of channel conductance, $\mu_{C_{ij}}$		8.086×10^{-14} m^3/Pa·s
Correlation coefficient, ρ of X_{ij} and Y_{ij}		0.902
Mean of channel length		0.000178 mm
Mean of channel cross section area		2.295×10^{-4} mm^2

Table 12. Three reactions for the condition of the top boundary inflow.

	Reactions	$\log K_{eq}$
1.	$H_2O \Leftrightarrow H^+ + OH^-$	-13.2
2.	$H_2CO_3^* \Leftrightarrow HCO_3^- + H^+$	-6.15
3.	$HCO_3^- \Leftrightarrow CO_3^{2-} + H^+$	-10.0

Table 13. Initial state of pores. pH is 6.6.

Species	concentration (M)	activity coeff.
H_2O	54.7	-
H^+	3.64×10^{-3}	0.686
OH^-	3.64×10^{-11}	0.686
Ca^{2+}	7.9×10^{-6}	0.221
Na^+	0.45	-
Cl^-	0.45	-

Table 14. Composition of the injected fluid. CO_2 solubility is 2.0M and pH is 2.9.

Species	[·](M) at equilibrium	γ at equilibrium
H_2O	54.7	-
H^+	1.734×10^{-3}	0.686
H_2CO_3	1.998	1.0
HCO_3^-	1.734×10^{-3}	0.686
CO_3^{2-}	4.52×10^{-10}	0.221
OH^-	7.74×10^{-11}	0.686
Ca^{2+}	7.9×10^{-6}	0.221
Na^+	0.45	-
Cl^-	0.45	-

Fig. 21 shows the effective reaction rates of anorthite and kaolinite in the validation test. Under the modeling condition, anorthite dissolves with an effective reaction rate of 6.8×10^{-9} mol/m^{2}s in the steady state. The bulk kaolinite reaction is precipitation with a steady state effective reaction rate of -7.7×10^{-10} mol/m^{2}s. The magnitude of anorthite reaction rate of the steady state is roughly 10 times as large as that of kaolinite. This large reaction rate produces abundant Al^{3+} and H_4SiO_4, which derive

kaolinite to precipitate. The effective and volume-averaged reaction rates in the steady state are compared to those determined in [4] in Table 15. Since the network for the validation simulation depends on random generation, there will be differences with the published results of [4]. The discrepancy in steady state variables is acceptable. Fig. 22 shows histograms of pH, [Ca^{2+}], saturation indices, and reaction rates, which are comparable with those in [4].

Table 15. Effective reaction rates, R_N, volume-averaged reaction rates, $\bar{R}$, and the ratio $\beta = \bar{R}/R_N$. The result is compared with Li's.

	Anorthite(mol/m^2s)			Kaolinite(mol/m^2s)		
	$R_{N,A}$	$\overline{R_A}$	β_A	$R_{N,K}$	$\overline{R_K}$	β_K
Simulation result	6.8×10^{-9}	2.4×10^{-8}	3.5	-7.7×10^{-10}	2.4×10^{-12}	-0.0031
Li[4]	$\sim5.5\times10^{-9}$	$\sim1.2\times10^{-8}$	2.3	$\sim -7.5\times10^{-10}$	$\sim 1.4\times10^{-12}$	-0.0018

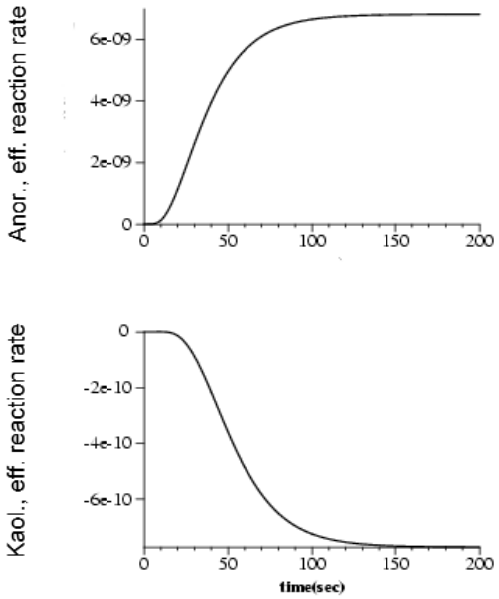

Fig. 21. Effective reaction rates (mol/m^{2}s) of anorthite and kaolinite.

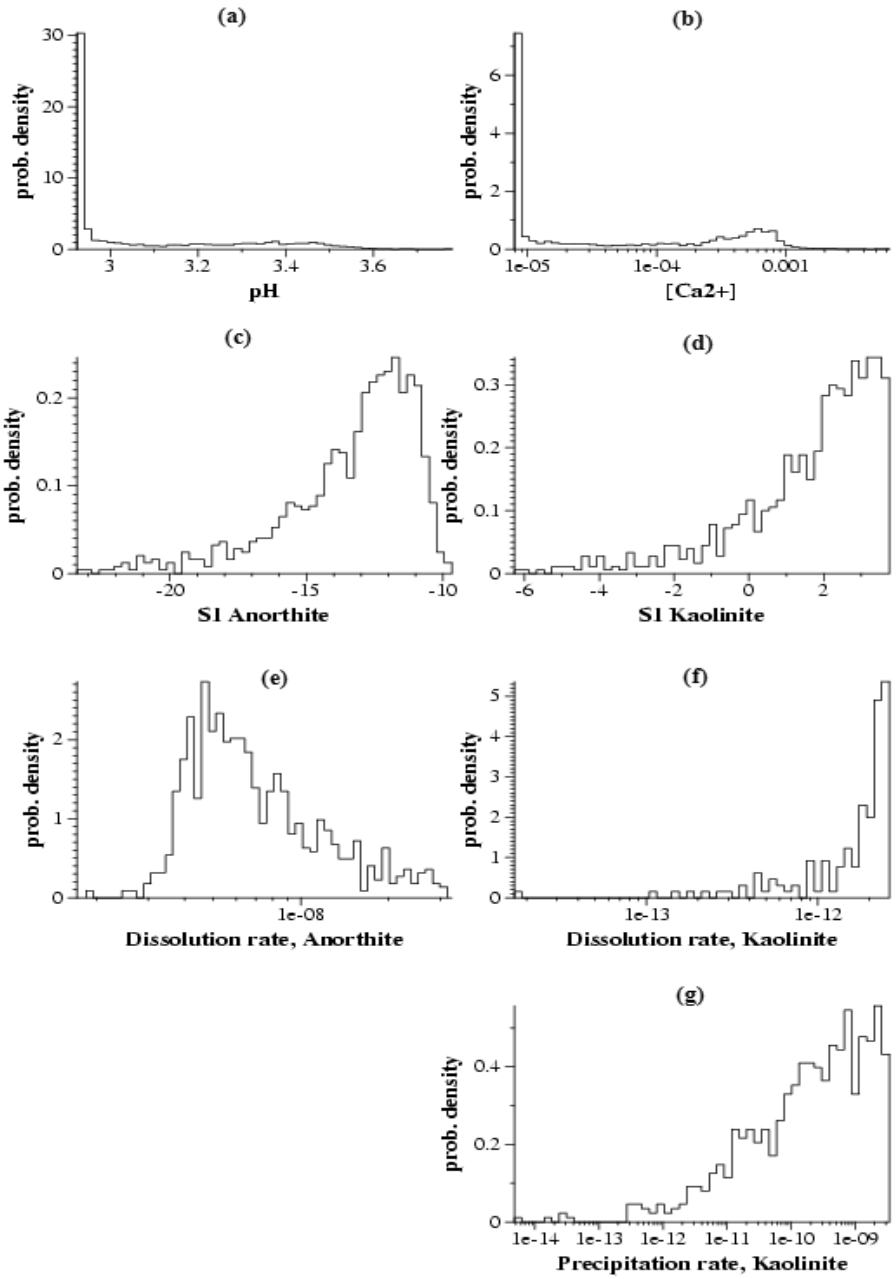

Fig. 22. Distributions by pore: (a) pH, (b) [Ca^{2+}], (c) saturation index of anorthite, SI_A, (d) saturation index of kaolinite, SI_K, (e) dissolution rate of anorthite (mol/m^2s), (f) dissolution rate of kaolinite (mol/m^2s), and (g) precipitation rate of kaolinite (mol/m^2s) in the steady state.

b. Application to Viking samples

The reactive flow simulation is performed in the network models based upon the Viking3W4 and Viking14W5 samples. The MoI surface area, (S_{RG}+S_{RB}) and the kaolinite surface area, S_{GB}, determined in Section 0.1 are used for the reactive anorthite and kaolinite surface areas, respectively.

Initial and boundary conditions are as described in Section II.4.c. The simulation condition is equivalent to case A in Li's simulation [4], except for the values of CO_2 solubility and volume flow rate. The solubility of CO_2 for the injected flow is computed by the method in Section II.4.d for P = 100 bar and T = 50 ^oC. The resulting solubility is 1.01 M, and the pH is 3.01. Concentrations in the injected solution are listed in Table 16.

Varying the flow rate allows for investigation of the dependence of bulk reaction rate on flow rate. If the flow rate is slow, the acidic saline water stays longer in a reactive pore. The anorthite reaction produces larger amounts of Al^{3+} and H_4SiO_4, and consumes more H^+ making conditions more favorable for kaolinite precipitation. Two average seepage velocities, v_{seep} = 0.0058 and 0.001 cm/s were selected for the simulations. The first value 0.0058 cm/s is the value from the validation study. A third velocity, v_{seep} = 0.0001 cm/s was also used for flow simulation through the Viking3W4 based network model to investigate kaolinite precipitation behavior at slow flow rates. The simulation cases are summarized in Table 17.

Table 16. Concentrations in the injected saline solution. CO_2 solubility of 1.01M and pH of 3.01.

Species	[·](M) at equilibrium	γ at equilibrium
H_2O	54.7	-
H^+	1.234×10^{-3}	0.686
H_2CO_3	1.012	1.0
HCO_3^-	1.234×10^{-3}	0.686
CO_3^{2-}	4.52×10^{-10}	0.221
OH^-	1.07×10^{-10}	0.686
Ca^{2+}	7.9×10^{-6}	0.221
Na^+	0.45	-
Cl^-	0.45	-

Table 17. Simulation cases.

Sample	v_{seep}(cm/s)	Simulation time	Case
Viking3W4	0.0058	976 sec.	1
	0.001	2000 sec.	2
Viking14W5	0.0058	9500 sec.	3
	0.001	10000 sec.	4
Viking3W4	0.0001	1386 sec.	5

Fig. 23 shows the bulk effective and volume-averaged reaction rates, R_N and $\bar{R}$ for cases 1 to 4. Fig. 24 shows the pore distribution of the saturation index (SI) and Fig. 25

shows bulk pH as a function of time. For these four cases, we discuss these figures together.

For the anorthite reactions (Fig. 23 (a) and (b)), the effective and volume-averaged reaction rates, $R_{N,A}$ and $\bar{R}_{\mathrm{A}}$, display the same behavior, rising monotonically to a steady state rate, with reasonable agreement between $R_{N,A}$ and $\bar{R}_{\mathrm{A}}$. For the seepage velocity of 5.8×10^{-3} cm/s (Fig. 23 (a)), the steady state for the anorthite reaction is reached in approximately 200 seconds (2 pore volumes), which is comparable with Li's [4] value, 100 seconds. Fig. 24 shows that the saturation state, Ω_{A} of anorthite of each pore is less than 10^{-10}, which makes $f_{\Omega} = 1 - \Omega^{m} = 1.0$ in (17). The reaction rate of anorthite is always towards precipitation and equal to f_{pH} by (17). Thus, pH is the only variable which determines the reaction rate of anorthite. The average pH of each case is shown in Fig. 25. The average pH increases rapidly after the injection of the acidic fluid and reaches to a steady state value after 2~3 pore volumes. Fig. 23 (a) and (b) show that $R_{N,A}$ has the same behavior as the average pH.

In Li's result [4], the effective reaction rate, $R_{N,K}$, for kaolinite decreases to a steady state, and reaches steady state around 100 seconds. In contrast to Li's simulation, $R_{N,K}$ initially rises (Fig. 23 (c), (d), and (e)) until the anorthite reaction reaches steady state, after which $R_{N,K}$ drops to (what appears to be approaching) a steady state value. The reasons for this are the following. The early-time behavior of the kaolinite reaction is governed by the pH change due to the acidic injected fluid. The f_{pH} term in (17) is increased by the acidic inflow (Fig. 6), increasing the kaolinite dissolution. When the bulk pH equilibrates, the kaolinite reaction rate is then controlled by the f_{Ω} term in (17) which is determined by $[Al^{3+}]$ and $[H_4SiO_4]$ produced by the anorthite reaction. This production of Al^{3+} and H_4SiO_4 slowly reduces the net dissolution of kaolinite by decreasing f_{Ω}.

Fig. 23 (e) shows that $R_{N,K}$ reaches steady state around 10^4 seconds for case 3 and after 10^4 seconds for case 4. The first reason for this long time to steady state for the kaolinite reaction rate is the small reactive surface area of anorthite in the rock network. The anorthite reaction produces Al^{3+} and H_4SiO_4 which induce the kaolinite precipitation. Thus, it requires more time for the anorthite reaction to produce sufficient Al^{3+} and H_4SiO_4 for kaolinite precipitation and subsequent achievement of steady state because of the small reactive surface area of anorthite. The total reactive surface area of anorthite is around 1% of the total surface area for both Viking3W4 and Viking14W5 in comparison to the 5% surface area in Li's network [4]. Furthermore, the specific surface area, S/V of the real rock network is 4×10^4 cm^{-1}, about half that of Li's network (9×10^4 cm^{-1}). Thus, the "specific anorthite reactive surface area", S_A/V of the rock network is approximately one-tenth as large as that of Li's network. The second reason is the difference in distribution of reactive surfaces of anorthite and kaolinite. In Li's network, 10% of the pores are reactive and each reactive pore contained equal surface areas of anorthite and kaolinite. The Al^{3+} and H_4SiO_4 produced by the anorthite reaction are therefore in the vicinity of all the kaolinite in the network and induce kaolinite precipitation immediately. Therefore in Li's simulation [4], the effective reaction rate of kaolinite is precipitation as soon as the simulation starts. In the network models for Viking3W4 and Viking14W5, only 20% of pores of Viking3W4 and 24% of pores of Viking14W5 contact anorthite while almost all pores contain kaolinite. In other words, there are 80% and 76% pores which have only kaolinite reactive surface areas. The kaolinite reaction in those pores is not immediately affected by the anorthite reaction and is affected only after Al^{3+} and

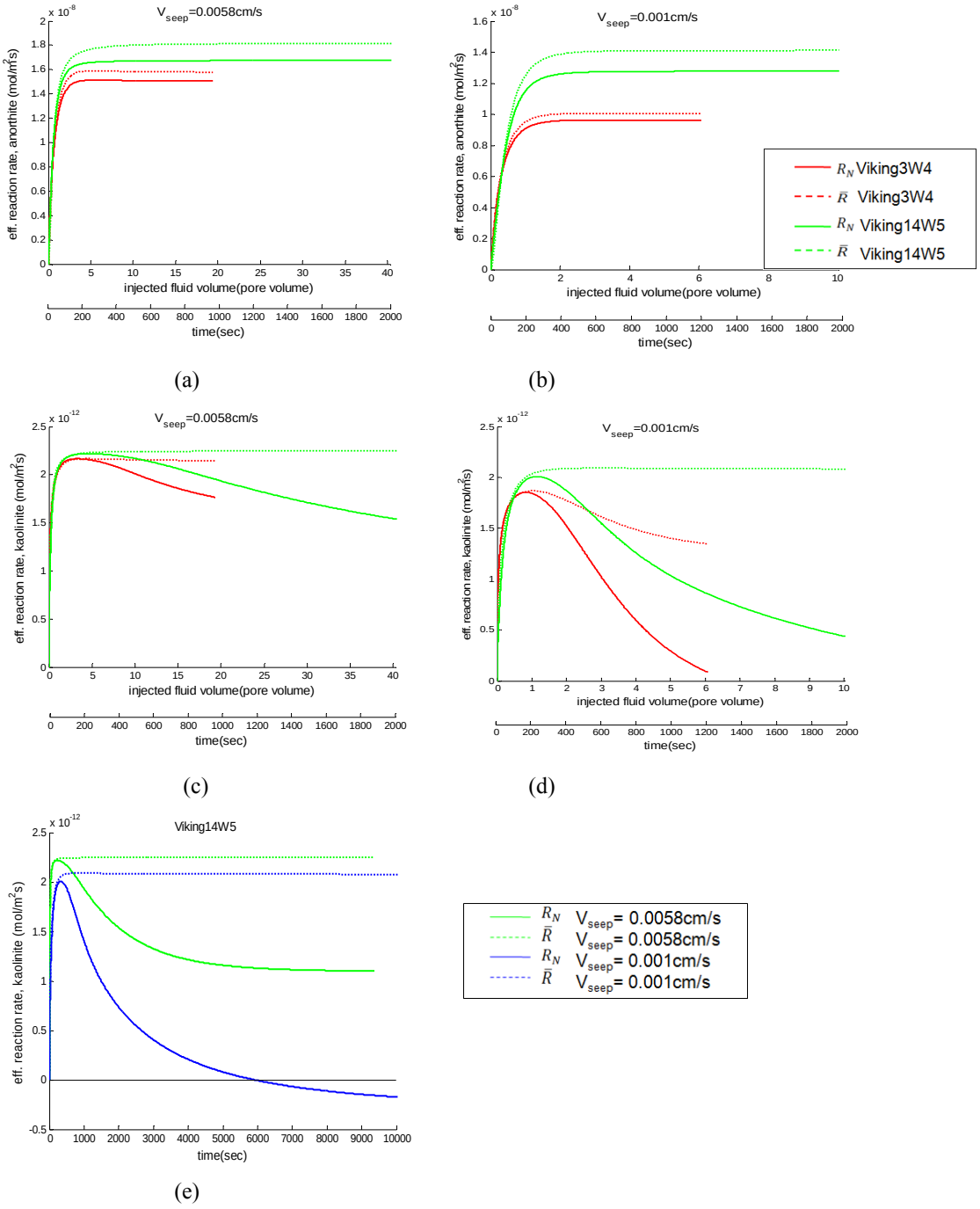

Fig. 23. Effective (solid lines) and volume-averaged (dotted lines) reaction rates of Viking3W4 (red) and Viking14W5 (green) between 0 sec. and 2000 sec. (a) reaction rates of anorthite with v_{seep} = 0.0058 cm/s (b) v_{seep} = 0.001 cm/s (c) reaction rates of kaolinite with v_{seep} = 0.0058 cm/s (d) v_{seep} = 0.001 cm/s. The reaction ratio, β, is given at the end time of each graph. (e) Effective reaction rates of kaolinite of Viking14W5 with v_{seep} = 0.0058 cm/s and v_{seep} = 0.001 cm/s from 0 sec. to 10000 sec. Four lines are identical to the green lines in (c) and (d).

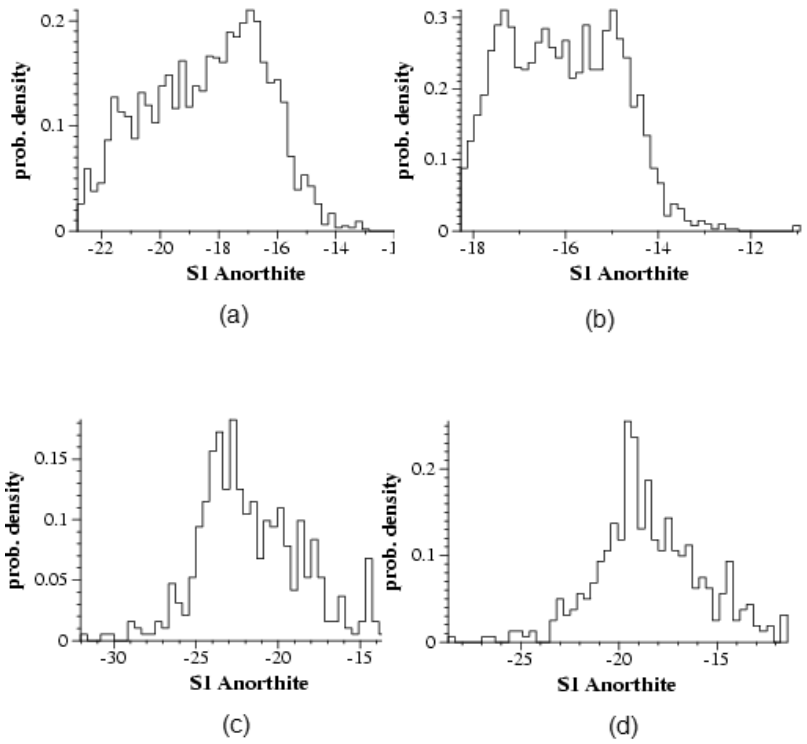

Fig. 24. Distributions by pore of the saturation index (SI = log Ω). (a) case 1, (b) case 2, (c) case 3, and (d) case 4.

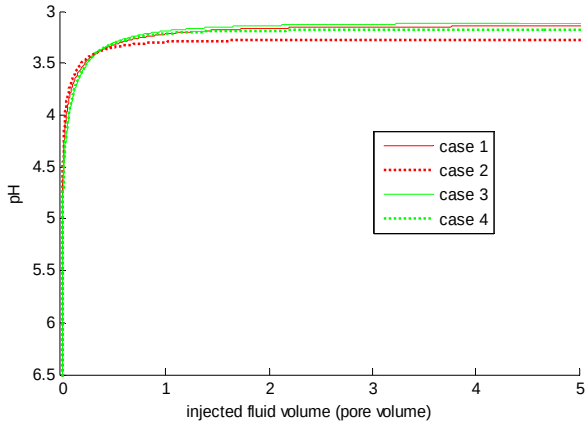

Fig. 25. Average pH vs. time for cases 1 – 4.

H_4SiO_4 produced by the anorthite reaction in other pores are appropriately transported. Furthermore to enable the kaolinite precipitation in upstream pores, Al^{3+} and H_4SiO_4 must be transported by only diffusion, which is slower than advection.

The ratio, β of volume-averaged reaction rate to effective reaction rate is an indicator of pore scale heterogeneities in the reaction rate. Equation (17) shows that the heterogeneities in the reaction rates are produced by heterogeneities in pH and Ω. Thus, the heterogeneities in the reaction rates can be analyzed by inspecting the heterogeneities in pH and Ω.

R_N, $\bar{R}$, and β of all cases are summarized in Table 18. The reaction ratio, β_A, of anorthite is close to 1.0 (between 1.0 and 1.1), which means the pore scale effect on the anorthite reaction is small. Fig. 23 (a), and (b) show reasonable agreement between the effective and volume-averaged reaction rates of anorthite. Since the saturation state, Ω_A, of anorthite is less than 10^{-10}, $r_A = f_{pH,A} \times f_{\Omega,\mathrm{A}} = f_{pH,A} \times (1 - \Omega_A) = f_{pH,A}$. In (12) the

Table 18. Simulation result of the effective and volume-averaged reaction rates. The reaction rates are computed at the times given in the table.

		v_{seep}(cm/s)	Anorthite(mol/m^{2}s)			Kaolinite(mol/m^{2}s)		
			$R_{N,A}$	$\overline{R_A}$	$\boldsymbol{\beta_A}$	$R_{N,K}$	$\overline{R_K}$	$\boldsymbol{\beta_K}$
Viking 3W4	Case 1	0.0058	1.51×10^{-8}	1.58×10^{-8}	**1.05**	1.68×10^{-12}	2.15×10^{-12}	**1.28**
	Case 2	0.001	9.62×10^{-9}	1.00×10^{-8}	**1.04**	-5.12×10^{-14}	1.31×10^{-12}	**-25.6**
Viking 14W5	Case 3	0.0058	1.68×10^{-8}	1.82×10^{-8}	**1.08**	1.10×10^{-12}	2.25×10^{-12}	**2.04**
	Case 4	0.001	1.28×10^{-8}	1.41×10^{-8}	**1.10**	-2.60×10^{-13}	2.08×10^{-12}	**-8.0**
Viking 3W4	Case 5	0.0001	3.14×10^{-9}	3.23×10^{-9}	**1.03**	-9.69×10^{-12}	-8.76×10^{-12}	**0.90**

dominant term in f_{pH} is $k_{H,A}\{H^+\}^{1.5}$ since $k_{H,A}$ and $\{H^+\}$ are respectively larger than $k_{OH,A}$ and $\{OH^-\}$ by a few orders of magnitude (Table 1). Thus, $r_A \sim k_{H,A}\{H^+\}^{1.5}$ and the distributions of pH and the anorthite reaction rate (Fig. 26 and Fig. 27) are similar (accounting for the fact that the pH plot is left-right reversed due to the negative sign in the definition of pH). Fig. 26 shows that the range of pH is narrow; this small variation of pH results in small heterogeneities in the anorthite reaction rate.

The ratios, β_K of the kaolinite reaction rate are also listed in Table 18. In cases 2 and 4, β_K values are -25.6 and -8.0, respectively, showing large pore scale effects while in cases 1 and 5, β_K's are 1.28 and 0.90 respectively. The dominant term in f_{pH} of the kaolinite reaction rate in (14) is $k_{H,K}\{H^+\}^{0.4}$, which is in the same form as the anorthite reaction rate, $r_A \sim k_{H,A}\{H^+\}^{1.5}$. Likewise, the pore scale effect on the kaolinite reaction rate by pH is small and thus, the pore scale effect is governed by the heterogeneities in $f_\Omega = 1 - \Omega^{0.9}$.

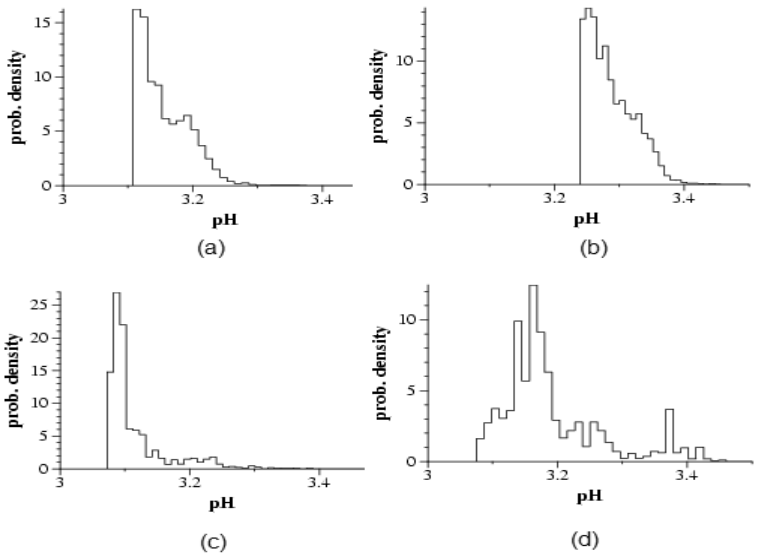

Fig. 26. pH distributions by pore. (a) Case 1, (b) case 2, (c) case 3, and (d) case4.

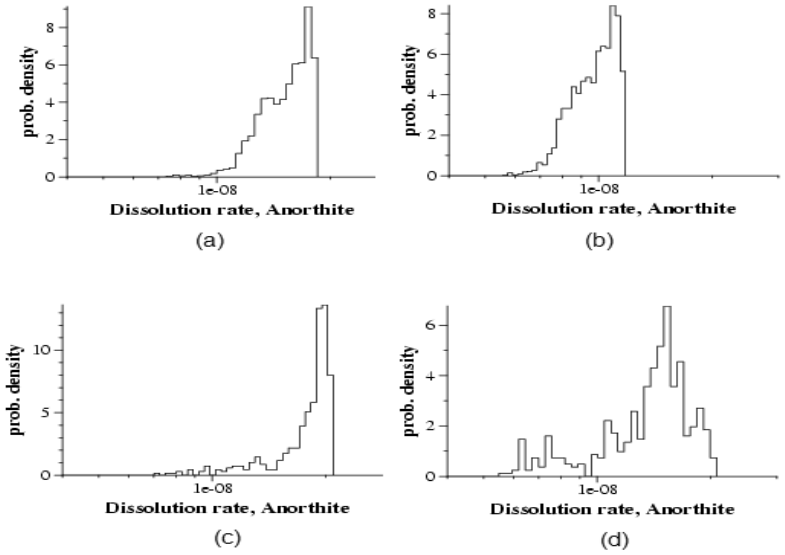

Fig. 27. Distributions of the anorthite reaction rate by pore. (a) Case 1, (b) case 2, (c) case 3, and (d) case 4.

The distributions of the kaolinite dissolution are shown in Fig. 28. Each distribution of the kaolinite dissolution has a sharp peak at the maximum rate and a tail in the negative direction. Cases 1 and 3 have sharper peaks and shorter tails than cases 2 and 4. Fig. 29 shows the distributions of the saturation index ($\mathrm{SI} = \log \Omega$) which affects the distribution of the kaolinite reaction. In cases 1 and 3 (Fig. 29 (a) and (c)), more than 70% of the SI values are less than -1; more than 70% of Ω_K values are less than 0.1. For these small values of Ω_K, $f_\Omega = 1 - \Omega^{0.9}$ is close to 1 and the dissolution rate is approximately equal to f_{pH} which is also almost constant. This constructs a peak in the distribution of the kaolinite dissolution and the peak is located around f_{pH}, which is also the maximum of the kaolinite dissolution since $f_\Omega \leq 1.0$ for the dissolution. A smaller number of other values of Ω_K between 0.1 and 1 determine f_Ω in the range from 0 to 0.9 and construct the tails in the distributions of the kaolinite dissolution.

The distributions of the kaolinite precipitation rate are also shown in Fig. 28. In case 2, the distribution is close to log-normal. In cases 3 and 4, the kaolinite precipitation rates are randomly distributed and this is because there are a small number of pores in which precipitation occurs. There are only 50 and 143 pores, respectively, in which kaolinite precipitation occurs in cases 3 and 4 respectively while there are 229 and 3159 pores in cases 1 and 2, respectively.

The maximum magnitude of f_Ω for the kaolinite dissolution is 1, but for the kaolinite precipitation, the magnitude of f_Ω is not bounded above. The kaolinite precipitation rate can therefore be amplified by f_Ω. For example, in cases 1-4, the maximum values for $\Omega_K^{0.9}$ are 665, 739, 230, and 195, producing $f_\Omega(\Omega_{K,max})$ = -664, -738, -229, and -194, respectively. The maximum magnitudes of f_Ω for the kaolinite precipitation rate are thus 664, 738, 229, and 194 times as large as those for the kaolinite dissolution rate. Consequently, in Fig. 28 the maximum precipitation rate (~5 $\times 10^{-10}$ mol/m^{2}s) is larger than the maximum dissolution rate (~2×10^{-12} mol/m^{2}s) by two orders as estimated by $f_\Omega(\Omega_{K,max})$. In each case, there are some large precipitation rate pores and this large variation of the kaolinite precipitation rate produces heterogeneities in the kaolinite reaction rate. In case 4, the bulk kaolinite reaction is precipitation solely due to the fact that although only 11% of the pores have kaolinite precipitation, these precipitation rates are very large.

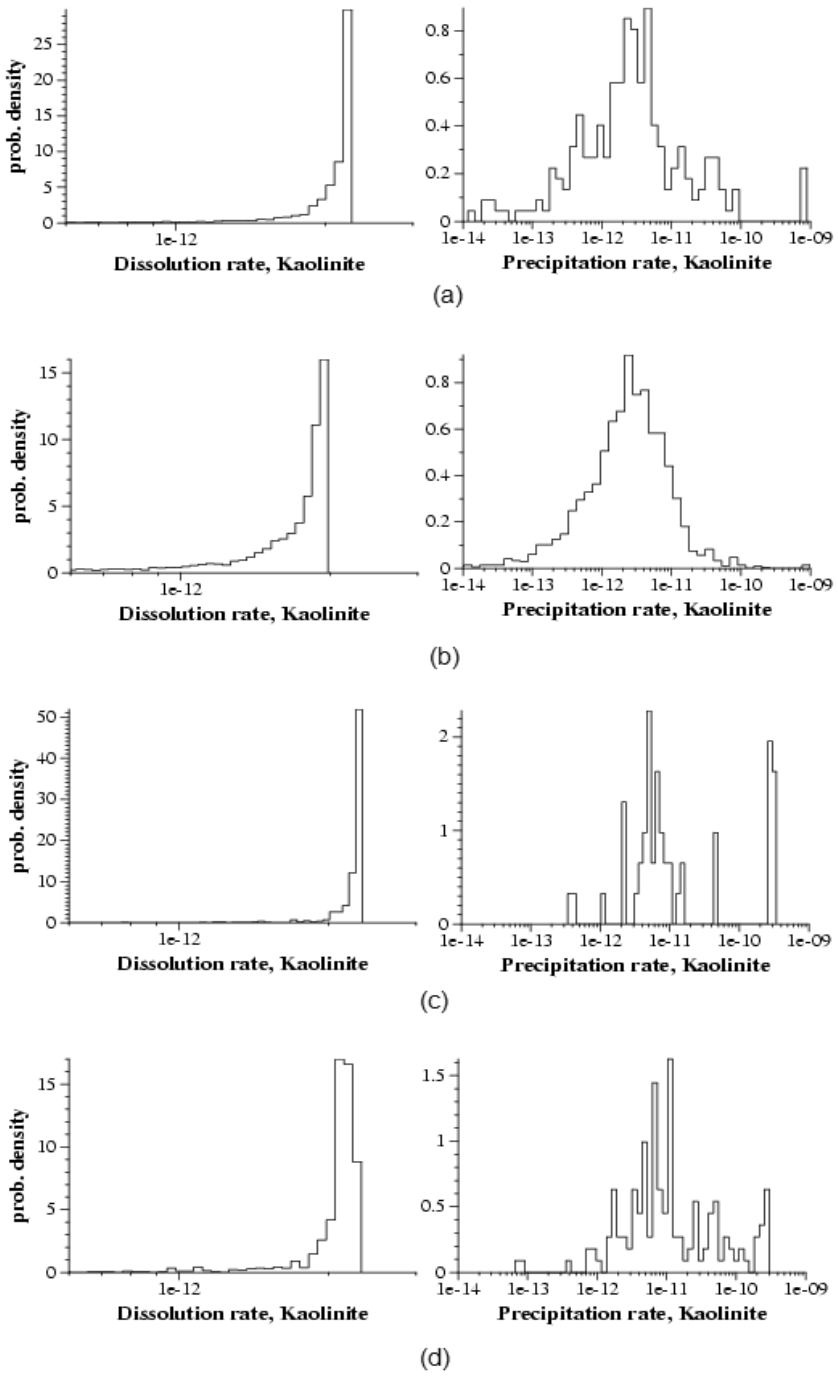

Fig. 28. Distributions of the kaolinite dissolution/precipitation rates by pore. (a) Case 1, (b) case 2, (c) case 3, and (d) case 4.

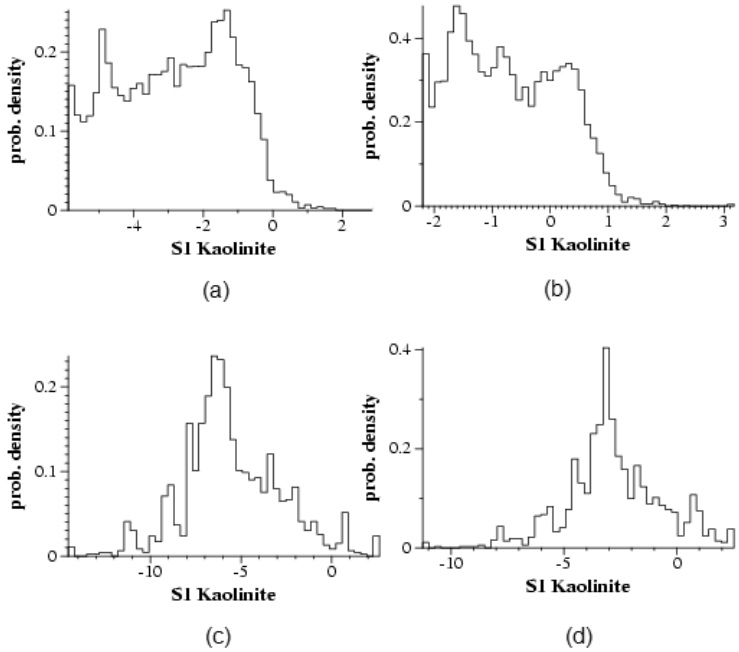

Fig. 29. Distributions of the saturation index of the kaolinite reaction by pore. (a) Case 1, (b) case 2, (c) case 3, and (d) case 4.

The volume-averaged reaction rate of kaolinite is computed using volume-averaged concentrations of $\overline{[H^+]}$, $\overline{[Al^{3+}]}$, and $\overline{[H_4SiO_4]}$. Large kaolinite precipitation rate pores do not however dominate the volume-averaged concentrations since a small number (<10%) of such pores do not govern the arithmetic averaging. The volume-averaged saturation state, $\bar{\Omega}_K \left(= \overline{\{Al^{3+}\}}^2 \overline{\{H_4SiO_4\}} / \overline{\{H^+\}}^6 K_{eq,K}\right)$ fails to reflect the large Ω_K values which produce the large precipitation rate. One way to quantify the heterogeneities in Ω_K is to compare the average, $\overline{f_\Omega}$, of f_Ω over the network with $f_\Omega(\bar{\Omega}_K)$. $\overline{f_\Omega}$ and $f_\Omega(\bar{\Omega}_K)$ imply the effect of f_Ω on the effective and volume-averaged reaction rates respectively. $\overline{f_\Omega}$ and $f_\Omega(\bar{\Omega}_K)$ are computed and compared in Table 19. $f_\Omega(\bar{\Omega}_K)$ predicts bulk dissolution for cases 1-4, but $\overline{f_\Omega}$ predicts bulk dissolution for cases

1 and 3 and bulk precipitation for cases 2 and 4. The ratio, β_K can be roughly predicted by the ratio, $f_\Omega(\bar{\Omega}_\mathrm{K})/\overline{f_\Omega}$. Therefore, the heterogeneities in kaolinite reaction rate can be explained by the heterogeneities in f_Ω and Ω_K.

Table 18 shows that the simulation results with v_{seep} = 0.001 cm/s (cases 2 and 4) have larger heterogeneities than the simulation of v_{seep} = 0.0058 cm/s (cases 1 and 3). The simulation result with the smallest seepage velocity, 0.0001 cm/s (case 5) has β_K of 0.9, which shows the smallest heterogeneities in the kaolinite reaction rate. Fig. 30 (a) and (b) show the small heterogeneities in both anorthite and kaolinite reaction rates in case 5. Fig. 30 (c) shows that SI_K is positive: all kaolinite reaction is precipitation. In case 5, most SI values are greater than 0.7 and thus, $\Omega_\mathrm{K} > 10^{0.7}$~5.0. For $\Omega_\mathrm{K} \gg 1$, $r_K = f_{pH} f_\Omega = f_{pH}\left(1-\Omega_K^{0.9}\right) \sim f_{pH}(-\Omega_\mathrm{K}^{0.9})$. This explains that the distribution of the kaolinite precipitation is similar to that of Ω_K. Fig. 29 (a) and (b) show that the size of the range of SI_K in cases 1 and 3 are approximately 8 and 5 respectively, but Fig. 30 (c) shows that the size in case 5 is 1.5. This small variation of Ω_K results in the small heterogeneities in the kaolinite reaction rate in case 5.

Table 19. Comparison of $\overline{f_\Omega}$ with $f_\Omega(\bar{\Omega}_\mathrm{K})$.

	Case	v_{seep}(cm/s)	$f_\Omega(\bar{\Omega})$	$\overline{f_\Omega}$	$f_\Omega(\bar{\Omega})/\overline{f_\Omega}$	β_K
Viking3W4	1	0.0058	0.566	0.25	0.83	1.28
	2	0.001	0.820	-0.14	-5.86	-25.6
Viking14W5	3	0.0058	1.00	0.25	4.00	2.04
	4	0.001	0.994	-0.48	-2.07	-8.00
Viking3W4	5	0.0001	-4.46	-7.14	0.62	0.90

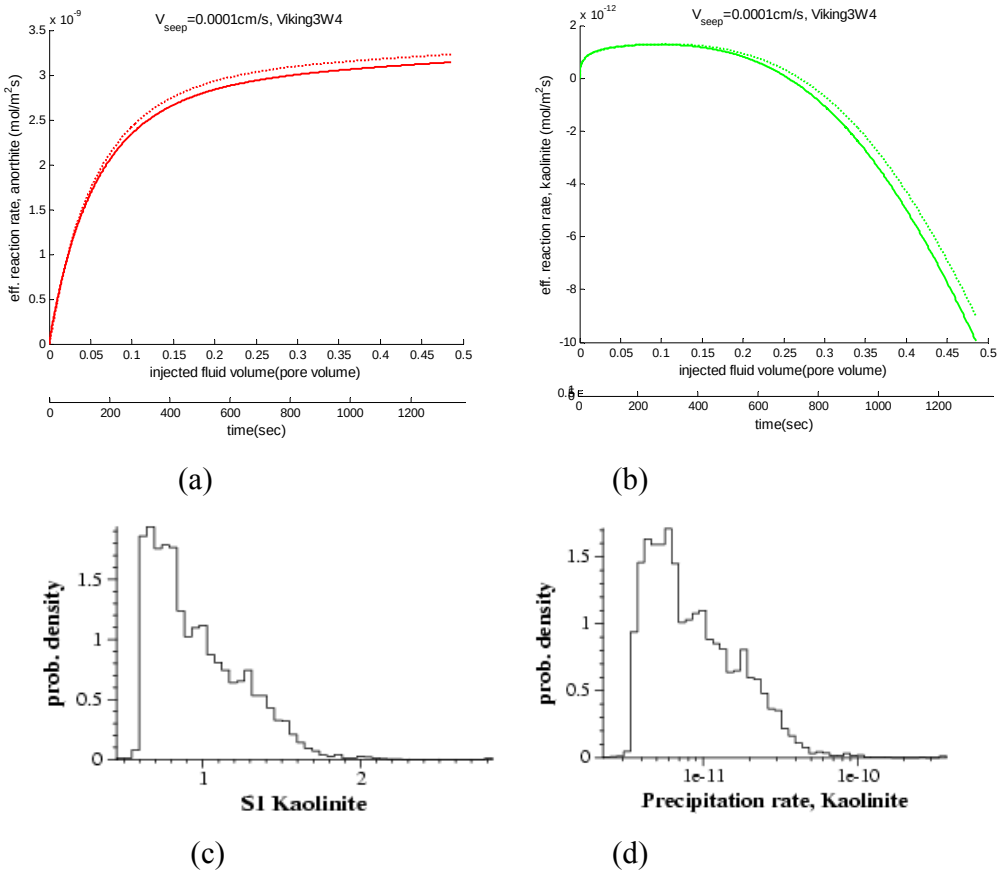

Fig. 30. Effective and volume-averaged reaction rates of (a) anorthite and (b) kaolinite from t = 0 to t = 1300 second. Distributions of (c) the saturation index of the kaolinite reaction and (d) the kaolinite precipitation rate. Case 5.

IV. Conclusion & future study

Mineral identification and pore-throat network construction of Viking samples are successfully completed, and the obtained result is reasonably acceptable and comparable with the BSE analysis. Reaction models are added to the network model to simulate reactive flow through the samples. The reactive transport model is validated by comparing the result with [4]. The network flow model is applied to Viking samples to compute the effective reaction rates and capture reaction heterogeneities which are impossible to capture without pore scale simulation. We can use the result for further analyses such as macro scale simulation of CO_2 sequestration and estimation of geological CO_2 storage capacity.

The behaviors of the reaction rates are very different from the result of previous research [4], and it also depends on the volume flow rate of the injected fluid. The time scale for the simulation is on the order of 1000 seconds while that of the previous paper [4] is approximately 100 seconds. The simulation results are analyzed to find the effect of reaction model on the reaction heterogeneities. While the anorthite reaction rate does not have large heterogeneities, the kaolinite reaction rate has large heterogeneities. The heterogeneities in the kaolinite reaction rate are influenced by the term, $f_\Omega = 1 - \Omega^{0.9}$ in the kaolinite reaction model. This term amplifies the kaolinite precipitation rate up to 700 times, and this results in the heterogeneities in the kaolinite reaction rate.

However, there are a few future topics required for more accurate, efficient simulation. First, the pore structure change by dissolution and precipitation is required for a more accurate simulation. By dissolution and precipitation of the two kinetic reactions,

the network structure can be transformed and thus, the transport property and mineral distributions can be changed. Second, MoI phase covered by kaolinite is partially accessible. The kaolinite is permeable, but it is less permeable than void phase. In the full temporal scale of CO_2 sequestration, the MoI covered by kaolinite is completely accessible, but in a short temporal scale, it may not be accessible. A model for the partial permeable property through kaolinite to access MoI is another future study. Third, the computation time of the simulation increases proportionally to the number of pores, and the simulation of Viking3W4 which has the largest number of pores requires too much computation time; the number of time steps is approximately one million. A new scheme such as implicit time integration is needed to reduce the number of time steps. Another approach for fast simulation is to parallelize the code. Next, we need a careful study on the kaolinite reaction rate model which allows an extremely large precipitation rate. The experiment [36] for the kaolinite reaction rate model does not include the range of large values of Ω. Finally, additional reaction models with minerals other than anorthite and kaolinite are another key to improve the simulation result. The MoI phase has many other minerals, and so, there are possibly some other important kinetic reactions which should be included in the network flow simulation.

Bibliography

1. *Basic Research Needs for Geosciences: Facilitating 21st Century Energy Systems*. 2007. Bethesda, MD.

2. Strazisar, B.R., C. Zhu, and S.W. Hedges, *Preliminary modeling of the long-term fate of CO_2 following injection into deep geological formations.* Environmental Geosciences, 2006. **13**: p. 1-15.

3. Piri, M., J.H. Prevost, and R. Fuller, *Carbon Dioxide Sequestration in Saline Aquifers: Evaporation, Precipitation and Compressibility Effects.* Fourth annual conference on carbon capture and sequestration DOE/NETL, 2005.

4. Li, L., C.A. Peters, and M.A. Celia, *Upscaling geochemical reaction rates using pore-scale network modeling.* Advances in Water Resources, 2006. **29**: p. 1357-1370.

5. White, A.F. and S.L. Brantley, *The effect of time on the weathering of silicate minerals: why do weathering rates differ in the laboratory and field?* Chemical Geology, 2003. **202**: p. 479-506

6. Kang, Q., P.C. Lichtner, and D. Zhang, *Lattice Boltzmann pore-scale model for multicomponent reactive transport in porous media.* Journal of Geophysical Research, 2006. **111**.

7. Li, L., C.A. Peters, and M.A. Celia, *Effects of mineral spatial distribution on reaction rates in porous media.* Water Resources Research, 2007. **43**.

8. Lichtner, P.C. and Q. Kang, *Upscaling pore-scale reactive transport equations using a multiscale continuum formulation.* Water Resources Research, 2007. **43**.

9. Kang, Q., P.C. Lichtner, and D. Zhang, *An improved lattice Boltzmann model for multicomponent reactive transport in porous media at the pore scale.* Water Resources Research, 2007. **43**.

10. Kang, Q., D. Zhang, and S. Chen, *Simulation of dissolution and precipitation in*

porous media. Journal of Geophysical Research, 2003. **108**.

11. Jin, G., T.W. Patzek, and D.B. Silin, *Direct Prediction of the Absolute Permeability of Unconsolidated and Consolidated Reservoir Rock.* Society of Petroleum Engineers (SPE90084), 2004.

12. Yiotis, A.G., et al., *A lattice Boltzmann study of viscous coupling effects in immiscible two-phase flow in porous media.* Colloids and Surfaces A: Physicochemical and Engineering Aspects, 2006. **300**: p. 35-49.

13. Lindquist, W.B., *3DMA General Users Manual*. 1999, Department of Applied Mathematics and Statistics, State University of New York at Stony Brook.

14. Lindquist, W.B. and A. Venkatarangan, *Investing 3D geometry of porous media from high resolution images.* Physics and Chemistry of the Earth, Part A:Solid Earth and Geodesy, 1999. **25**: p. 593-599.

15. Lindquist, W.B., et al., *Pore and throat size distributions measured from synchrotron X-ray tomographic images of Fontainebleau sandstone.* Journal of Geophysical Research, 2000. **105**: p. 21,509-21,527.

16. Shin, H., et al., *Analysis of the vesicular structure of basalts* Computers and Geosciences, 2005. **31**(4): p. 473-487.

17. Oh, W. and W.B. Lindquist, *Image threshing by indicator kriging.* IEEE Transcations on Pattern Anaysis and Machine Intelligence, 1999. **21**(7): p. 590-602.

18. Seright, R.S., M. Prodanovic, and W.B. Lindquist, *X-Ray Computed Microtomography Studies of Fluid Partitioning in Drainage and Imbibition Before and After Gel Placement: Disproportionate Permeability Reduction.* Society of Petroleum Engineers (SPE89393), 2004.

19. Peters, C.A., D. Kim, and W.B. Lindquist, *Mineral Distribution Analysis via BSE, EDX, and CMT.* in preparation.

20. Lee, T.C., R.L. Kashyap, and C.N. Chu, *Building skeleton models via 3D medial surface/axis thinning algorithm.* CVGIP:Graph Models Image Process, 1994: p. 462-478.

21. Prodanovic, M., *Fluid Displacement in Rock Cores: A Study Based on Three Dimensional X-ray Microtomography Images*, in *Applied Mathematics and Statistics*. 2005, Stony Brook University.

22. Silin, D.B., G. Jin, and T.W. Patzek, *Robust Determination of the Pore Space Morphology in Sedimentary Rocks (SPE 84296).* Society of Petroleum Engineers, 2003.

23. Lorensen, W.E. and H.E. Cline, *Marching cubes: A high resolution 3-D surface construction algorithm.* ACM Computer Graphics, 1987. **21**: p. 163-169.

24. Lohmann, G., *Volumetric Image Analysis*. 1998: John Wiley & Sons and B. G. Teubner Publishers.

25. Brunauer, S., P.H. Emmet, and E. Teller, *Adsorption of Gases in Multimolecular Layers.* Journal of the American Chemical Society 1938. **60**: p. 309-319.

26. Patzek, T.W., *Verification of a Complete Pore Network Simulator of Drainage and Imbibition.* Society of Petroleum Engineers (SPE59312), 2000.

27. Sholokhova, Y., D. Kim, and W.B. Lindquist, *Network Flow Modeling via Lattice-Boltzmann Based Channel Conductance.* Journal of Colloid and Interface Science, submitted.

28. Harr, M.E., *Ground water and seepage*. 1990: Dover Publication.

29. Skalicky, T., *LASPack Reference Manual.* Institute for Fluid Mechanics, Dresden University of Technology, 1995.

30. Trefethen, L.N. and D. Bau, *Numerical Linear Algebra*. 1997: Society for Industrial and Applied Mathematics.

31. White, F.M., *Viscous Fluid Flow*. 2nd ed. Mechanical Engineering Series. 1991: McGraw-Hill.

32. Mason, G. and N.R. Morrow, *Capillary behavior of a perfectly wetting liquid in irregular triangular tubes.* Journal of Colloid and Interface Science, 1991. **141**: p. 262-274

33. Oren, P.E., S. Bakke, and O.J. Arntzen, *Extending predictive capillities to network models.* Society of Petroleum Engineers, 1998.

34. Bourbie, T. and B. Zinszner, *Hydraulic and Acoustic Properties as a Function of Porosity in Fontainebleau Sandstone.* Journal of Geophysical Research, 1985. **90**: p. 11524-11532.

35. Chapra, S.C. and R.P. Canale, *Numerical Methods for Engineers*. 1988: McGraw-Hill.

36. Nagy, K.L., A.E. Blum, and A.C. Lasaga, *Dissolution and precipitation kinetics of kaolinite at 80°C and pH 3: The dependence on solution saturation state.* American Journal of Science, 1991. **291**: p. 649-686.

37. Benjamin, M.M., *Water Chemistry*. McGraw-Hill Series in Water Resources and Environmental Engineering. 2002: McGraw-Hill.

38. Johnson, J.W., E.H. Oelkers, and H.C. Helgeson, *SUPCRT92: A software package for calculating the standard molal thermodynamic properties of minerals, gases, aqueous species, and reactions from 1 to 5000 bar and 0 to 1000°C.* Computers & Geosciences, 1992. **18**: p. 899-947.

39. Conte, S.D. and C.d. Boor, *Elementary Numerical Analysis*. 1980: McGraw-Hill.

40. Duan, Z. and R. Sun, *An improved model calculating CO_2 solubility in pure water and aqueous NaCl solutions from 273 to 533 K and from 0 to 2000 bar.* Chemical Geology, 2003. **193**: p. 257-271.

41. Millero, F.J., *Physical Chemistry of Natural Waters*. Wiley-Interscience Series in Geochemistry. 2001: Wiley-Interscience.

42. Cussler, E.L., *Diffusion:mass transfer in fluid system*. 2 ed. 1997: Cambridge University Press.

43. Tsuchiyama, A., *Quantitative evaluation of attenuation contrast of minerals by using a medical X-ray CT scanner.* Journal of Mineralogical and Petrological Sciences, 2000. **95**: p. 125-137.